Crystal Power:
Piezo Coupling to the Quantum Zero Point

L. J. November

La Luz Physics, La Luz NM 88337-0217, USA

E-mail: laluzphys@yahoo.com

18 April 2011

Abstract. We consider electro-optical constructions in which the Casimir force is modulated in opposition to piezo-crystal elasticity, as in a stack of alternating tunably conductive and piezo layers. Adjacent tunably conducting layers tuned to conduct, attract by the Casimir force compressing the intermediate piezo, but when subsequently detuned to insulate, sandwiched piezo layers expand elastically to restore their original dimension. In each cycle some electrical energy is made available from the quantum zero point (zp). We estimate that the maximum power that could be derived at semiconductor THz modulation rates is megawatts/cm^3 !

Similarly a permittivity wave generated by a THz acoustic wave in a single crystal by the acousto-optic effect produces multiple coherent Casimir wave mode overtones and a bulk mode. We model the Casimir effect in a sinusoidally graded medium finding it to be very enhanced over what is found in a multilayer stack for the equivalent permittivity contrast, and more slowly decreasing with scale, going as the wavelength $1/\lambda^2$. Acoustic waves give comparable theoretical power levels of MW/cm^3 below normal crystal damage thresholds. Piezo thermodynamic relations give conditions for effective coupling of the Casimir bulk mode to an external electrical load. Casimir wave modes may exchange energy with the main acoustic wave too, which may partially account for THz attenuation seen in materials. We outline feasibility issues for building a practical crystal power generator.

PACS numbers: 77.65.Dq, 78.20.hb, 42.50.Pq, 43.25.Ed

1. Introduction

Though it is well accepted conceptually that the lowest energy quantum state contains energy, the quantum zero-point (zp) or vacuum fluctuation energy seems regarded somewhat distrustfully by many physicists as a *real* energy. The zp energy seems indispensable in the self-consistent formulation of many different physical processes: pair creation and annihilation, spontaneous emission, the Lamb shift, electron fluctuations, black-body radiation, van der Waals particle, and vacuum cavity forces (see Milonni's excellent overview book [1]), but the possibility that it could provide a significant energy transfer for human use gets too close to looking like a violation of energy conservation, getting something for nothing, or perpetual motion. Though zp energy is well accepted

as the source for the synthesis of the universe out of nothing in the big bang by pair creation [2] with enhancement effects possible in dynamical expansion processes [3], its importance in more common physical processes seems less acceptable. Still methods that may give a significant transfer of energy out of the quantum vacuum for practical utilization have been shown to be theoretically possible [4], and possible implementations are being discussed and explored [5, 6, 7].

Vacuum cavity forces, especially in the example of the Casimir effect, give a macroscopic manifestation of the zp energy. Casimir [8, 9] showed that large-area closely spaced parallel conducting plates in a vacuum exhibit a force of attraction, which arises due to the distribution of electromagnetic fluctuations in the quantum zp field introduced by the conductors. We might suppose that the Casimir force is conservative like gravity, and parallel conducting plates should lose in their separation whatever mechanical energy was obtained by their attraction. However, it seems that this is really not the case: We know that the Casimir force can be turned on or off as tunably conductive plates are changed to conduct or insulate. If parallel tunably conductive plates operate elastically as against a spring between them, the work done in the attraction of the plates when the Casimir effect is turned on need *not* be returned in their subsequent separation when the Casimir effect is turned off. That excess of energy might be harvested, in effect, taking energy out of the quantum zp. The modulation of the Casimir effect by the conductive cycling of semiconductors with laser light has been demonstrated in precise differential tests, which have validated the theoretical estimates to within 1% [10, 11].

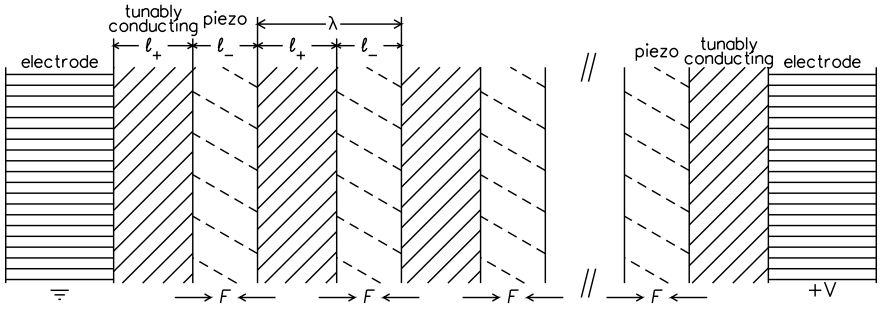

Figure 1. Thought Experiment: Multilayer stack of alternating tunably conductive and piezo layers. Changing the tunably conductive layers to conduct and then insulate produces a Casimir compression followed by its elastic reexpansion, which does net work on the piezo crystals from which useful electrical energy might be derived.

To understand the possibilities for energy extraction, we consider as an idealization a stack of alternating tunably conductive and piezo layers bounded by conducting electrodes as illustrated in Figure 1. The Casimir effect between two conductive layers produces a net attractive force per unit area F in the intermediate piezo layer that drops off rapidly with the increasing piezo layer thickness ℓ_-, so the piezo layers must be quite thin to obtain a strong effect. Sandwiching conductive plates separated by a small intermediate dielectric of permittivity ε_{e-} and thickness ℓ_- exhibit a near-field

Casimir force $F_\langle(\ell_-)$ that follows a $1/\ell_-^3$ power law up to some cross-over separation $\ell_{\langle\rangle}$, and then switches to a steeper $1/\ell_-^4$ power law, written for perfectly conducting infinite area bounding layers from the Lifshitz formulation [12]

$$F_\rangle = \frac{\pi^2\hbar c}{240\sqrt{\varepsilon_{e-}}\ell_-^4} = \left[\frac{270\text{ nm}}{\ell_-}\right]^4 \text{dyn/cm}^2, \tag{1}$$

where the static permittivity of the piezo layer is ε_{e-}; as usual $\hbar$ is Planck's constant over 2π and c the speed of light. For the rightmost equality, a static permittivity of ε_{e-}=6 (index-of-refraction squared) was used for moderate-index insulators, and gives a Casimir force per unit area of just 1 dyn/cm^2 or 1 erg/cm^3 = 1E−7 Joules/cm^3 for the piezo thickness ℓ_- = 270 nm (using the 'E' notation for the power of 10). Though the Lifshitz solution is for infinitely thick sandwiching plates, his solution represents a good approximation too when the plates are comparable in thickness to their separation $\ell_+ \sim \ell_-$, as we discuss. The cross-over separation where the power law switches to $1/\ell_-^3$ is characteristically less than 7 nm for near conducting sandwiching layers, as we elaborate in Appendix A.

In acting against an intermediate elastic material, the attractive force per unit area F produces a dimensionless strain $-sF$ or a compressional displacement $sF\ell_-$ in a layer of thickness ℓ_-, where s is the material elastic compliance for the stress component in the forcing direction. The average work done per unit area by the Casimir force in compressing the intermediate layer by a continuous motion is the integral through a half cycle of the force F times the infinitesimal displacement $s\ell_-\partial F$ or $s\ell_-F^2/2$ for F the maximum force in the cycle, giving the total work done per unit of time and volume

$$W = \frac{1}{4}s\nu F^2, \tag{2}$$

for cycling at a rate ν, and supposing equal odd-even layer thicknesses $\ell_+ = \ell_-$, so half of the volume participates in the compression at any time. This formula is an approximate form useful for estimating the amplitude of the effect, as it supposes the idealization of high piezo efficiency, a static piezo response, and ignores contributions from the converse piezo effect, as we elaborate in Section 6.

Semiconductor modulation at rates up to about ν=1E13 Hz by electrical modulation in adjacent oppositely doped layers for modern transistor design has been demonstrated [13]. Material compliances range from about $s \sim$1E−7 to 1E−12 Pa^{-1} for soft rubber to the hardest crystals like diamond. For estimating the amplitude of the effect, we suppose most conservatively $s \sim$ 1E−12 Pa^{-1} = 1E−13 cm^2/dyn, and obtain a power per unit volume W=0.25 erg/s/cm^3 in a stack with layer thickness ℓ_- = 270 nm from (2). As the power scales inversely as ℓ_-^8, with a tenth that layer thickness ℓ_-=27 nm, we obtain a much larger W=2.5 Watts/cm^3, and for ℓ_-=5 nm, W=1.8 megawatts (MW)/cm^3 ! Actually the estimate is somewhat high for normal good conductors, which fall significantly short of the ideal of perfect conductivity. Still our more careful estimate gives power up to megawatts/cm^3 for idealized stacks of alternating tunably conducting and piezo layers, as we discuss in Section 4. Physical constructs could be possible as we elaborate in the text as deposition of layers only ℓ_-=5 nm, about 10 molecular layers

in thickness, are reached in microlayer nanotechnology, like what is used in integrated circuits.

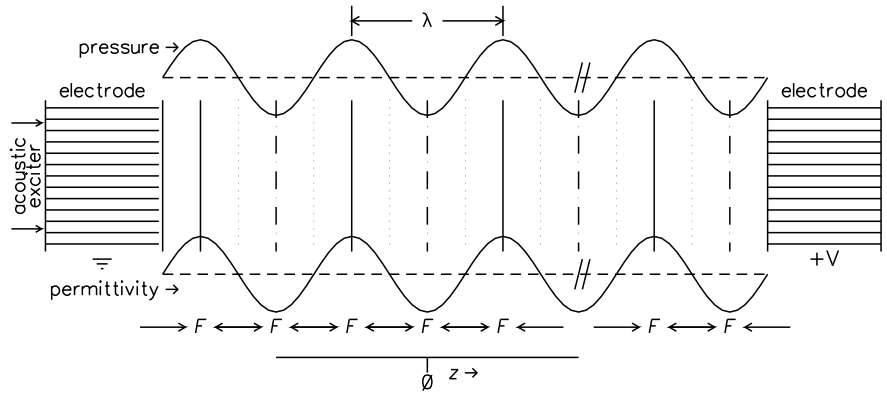

Figure 2. ZP energy from a standing acoustic wave in a piezo crystal. Successive close permittivity plane wave fronts introduced by an acoustic wave interact like alternating layers, giving an added Casimir force that is modulated in time with the wave oscillation.

From the thought experiment, we recognize a basic physical principle and study processes that systematically modulate the Casimir effect, like a pressure wave standing or traveling, longitudinal or transverse, which produces a periodic sinusoidal permittivity variation by the acousto-optic effect, as illustrated in Figure 2. As with the alternating-layer stack, adjacent plane wave fronts in permittivity must interact via the Casimir effect giving an added longitudinal stress at the extremes of the temporal oscillation, as illustrated by the force vectors F. The Casimir effect in acoustic waves too may produce a voltage difference across a piezo crystal from which electrical power might be derived.

The Casimir effect in graded permittivity media has been considered mainly to understand effects of soft boundaries on three-layer solutions, and shown to exhibit quantum divergences unlike what is found for solutions with discrete layers, suggesting an enhanced effect [14, 15, 16]. We formulate the problem again for a general 1D spatial graded permittivity variation in Sections 2 and 3. Numerical models for stacks of alternating permittivity layers are presented in Section 4, and for permittivity waves in uniform media in Section 5. Besides being enhanced for the equivalent permittivity contrast, the Casimir effect also exhibits a much slower falloff with the scale of the variation than what is seen with discrete layers.

The zp energy dynamics are examined using the piezo thermodynamic relations in Section 6, which shows formally the transfer of energy out of or back into the quantum zp in the Casimir modulation of piezo crystals for certain acoustic wave conditions. Energy that is not used is cycled into and out of the quantum zp, with the strain and stress modulated in phase. Estimates for power production for alternating-layer stacks and acoustic waves in crystals from our numerical models are given in Section 7. Casimir wave modes may interact with the principle acoustic wave too to drive its attenuation or growth, as we discuss in Section 8. Some practical issues for design of a zp-power

harvester based upon acoustic waves in single uniform piezo crystals are discussed with conclusions in Section 9.

2. Casimir Effect with a 1D Permittivity Variation

The Casimir force arises in a medium with a 1D permittivity variation $\hat{\varepsilon}(\xi, z)$ in a spatial coordinate z as in the multilayer stack illustrated in Figure 1 or the single crystal in Figure 2. The general complex permittivity $\hat{\varepsilon}(\xi, z)$ characterizes fully the electro-optic properties of a medium, defining the index-of-refraction and absorption variations as a function of light frequency ξ. The Casimir force is derived in many places especially after the general Lifshitz formulation [12]. We write it as a force per unit area or a pressure as a function of z with positive as compressive

$$F(z) = \frac{k_{\mathrm{B}}\Theta}{\pi c^2} {\sum_{n=0}^{\infty}}' \int_0^{\infty} \varpi\kappa(z) \left(Д_s(z) + Д_p(z)\right) d\varpi, \tag{3}$$

for k_{B} Boltzmann's constant and Θ the temperature. The sum is over the Matsubara frequencies $\xi = n2\pi k_{\mathrm{B}}\Theta/\hbar = n[\Theta/300\mathrm{K}]$ 2.47E14 rad/s, where the integer index n counts the frequency intervals, and the prime on the summation indicates that the zero frequency $n = 0$ term receives half weight. The two terms $Д_{\binom{s}{p}}$ represent the Fresnel reflection variation for perpendicular s (senkrecht) and parallel p zp polarized rays defined

$$Д_{\binom{s}{p}}(z) = \frac{R_{\binom{s}{p}+}(z) R_{\binom{s}{p}-}(z)}{1 - R_{\binom{s}{p}+}(z) R_{\binom{s}{p}-}(z)}, \tag{4}$$

for Fresnel reflection coefficients $R_{\binom{s}{p}\pm}$, which depend upon the permittivity. The wavenumber $\kappa(z)$ is for zp dissipative electromagnetic modes and is defined in by the Matsubara sum and integration frequencies ξ and ϖ

$$\kappa(z) = \frac{1}{c} \left(\varepsilon(\xi, z)\xi^2 + \varpi^2\right)^{\frac{1}{2}}. \tag{5}$$

The definition for $\kappa(z)$ and Fresnel reflection coefficients $R_{\binom{s}{p}\pm}$ use the function $\varepsilon(\xi, z) \equiv \hat{\varepsilon}(i\xi, z)$, the projection of the complex permittivity on its imaginary frequency axis, which casts the complex $\hat{\varepsilon}$ into a real function ε consistent with Kramers-Krönig causality constraints [17]. This solution may be applied to represent index, absorption, conductivity, or magnetic permeability variations in a medium.

It is usual to replace the finite sum over Matsubara frequencies in (3) by an integral. Symbolically the sum might be approximated ${\sum_{n=0}^{\infty}}' \ldots \to \int_0^{\infty} \ldots dn$, which takes properly into account the half-size interval around the lower limit $n = 0$. Using the Matsubara formula with $d\xi = (2\pi k_{\mathrm{B}}\Theta/\hbar)dn$ gives on substitution the integral approximation for the Casimir force

$$F(z) = \frac{\hbar}{2\pi^2 c^2} \int_0^{\infty} \int_0^{\infty} \varpi\kappa(z) \left(Д_s(z) + Д_p(z)\right) d\varpi d\xi. \tag{6}$$

A general substitution for the sum that takes into account singularities in the complex permittivity function $\hat{\varepsilon}(i\xi)$ must include Cauchy principle values as represented by the

Abel-Plana formula [18]. The singularities in the complex function $\hat{\varepsilon}(i\xi)$ are on the positive real axis in its complex argument $i\xi$ and enclosed in the upper half plane of $i\xi$ by the infinite integral along the imaginary axis of $i\xi$, as contained in the sum over the real Matsubara frequencies ξ from zero to infinity in the formula (3). Simply substituting the integral for the sum represents a good approximation for all temperatures when the scales of variation are smaller than about 1 μm [19] as we illustrate in numerical models in Section 4.

Fresnel reflection coefficients $R_{\binom{s}{p}\pm}(z)$ for the relevant dissipative waves of wavenumber $\kappa(z)$ in the s and p polarizations are propagated by recursion on the left side $(-)$ from $R_{\binom{s}{p}-}(z) = 0$ as $z \to -\infty$ or on the right side $(+)$ from $R_{\binom{s}{p}+}(z) = 0$ as $z \to +\infty$. The left-side reflection coefficients $R_{\binom{s}{p}-}$ (or right-side $R_{\binom{s}{p}+}$) change moving a distance Δz (or moving $-\Delta z$ for the right-sided coefficients) to cross a permittivity jump at some z following the comprehensive formula [Section 1.6][20]

$$R_{\binom{s}{p}\pm}(z) = \frac{r_{\binom{s}{p}\pm}(z) + R_{\binom{s}{p}\pm}(z \pm \Delta z)e^{-2\kappa(z\pm\Delta z)\Delta z}}{1 + r_{\binom{s}{p}\pm}(z)R_{\binom{s}{p}\pm}(z \pm \Delta z)e^{-2\kappa(z\pm\Delta z)\Delta z}}, \tag{7}$$

with Δz always positive, where the coefficients for the jump at z, $r_{\binom{s}{p}\pm}(z)$, are defined by the relative differences

$$r_{s\pm}(z) = \frac{\kappa(z \mp \delta z) - \kappa(z \pm \delta z)}{\kappa(z \mp \delta z) + \kappa(z \pm \delta z)}, \tag{8}$$

$$r_{p\pm}(z) = \frac{\varepsilon(z \pm \delta z)\kappa(z \mp \delta z) - \varepsilon(z \mp \delta z)\kappa(z \pm \delta z)}{\varepsilon(z \pm \delta z)\kappa(z \mp \delta z) + \varepsilon(z \mp \delta z)\kappa(z \pm \delta z)}, \tag{9}$$

for any infinitesimal (positive) distance $\delta z < \Delta z$. We observe the sign convention that the differences are between the wavenumber nearer $z = 0$ minus the wavenumber further out, which leads to convenient solution symmetries. With no permittivity change over an interval Δz, the jump coefficients are zero $r_{\binom{s}{p}\pm} = 0$, and the Fresnel reflection coefficients decrease exponentially in $+z$ for the left-sided solutions $R_{\binom{s}{p}-}(z)$ or in $-z$ for the right-sided solutions $R_{\binom{s}{p}+}(z)$ with $R_{\binom{s}{p}\pm}(z) = R_{\binom{s}{p}\pm}(z \pm \Delta z)\exp(-2\kappa\Delta z)$. The formulae are relevant for reflection coefficients crossing discrete permittivity jumps, but are applicable in graded-media too, as we elaborate in the next section. We sometimes denote the variables as $\varepsilon_j(\xi)$ or κ_j using subscripts rather than functions of z for discrete layers counted from a middle layer $j = 0$ as illustrated in Figure 3. The $\pm$ subscript is also used for even and odd layers with alternating-layer stacks, where the reversed state is of special interest with interchanged permittivities $\varepsilon_+ \leftrightarrow \varepsilon_-$ and wavenumbers $\kappa_+ \leftrightarrow \kappa_-$.

For a symmetric permittivity variation $\varepsilon(z) = \varepsilon(-z)$, recursive application of the formula (7) gives $R_{\binom{s}{p}+}(z) = R_{\binom{s}{p}-}(-z)$, or for the product $R_{\binom{s}{p}+}(z)R_{\binom{s}{p}-}(z) = R_{\binom{s}{p}+}(-z)R_{\binom{s}{p}-}(-z)$, for $Д_{\binom{s}{p}}(z) = Д_{\binom{s}{p}}(-z)$ from (4), and a symmetric Casimir force in (3) or (6) with $F(z) = F(-z)$.

In a multielement stack or square permittivity wave, the Casimir force can be seen to be constant in every constant permittivity zone. The left/right-sided $(\mp)$ Fresnel

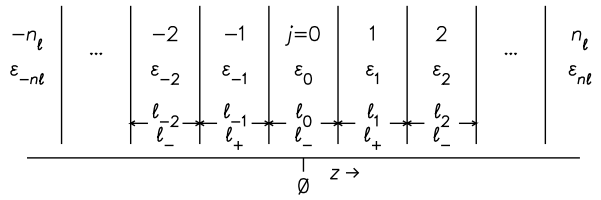

Figure 3. Plane-parallel multilayer sandwich with n_ℓ layers of differing permittivities on each side of a layer $j = 0$ of principle interest

reflection coefficients are propagated from bounding permittivity jumps at $z = \mp\ell_0/2$ to a given z in a middle layer of thickness ℓ_0 as in Figure 3 with

$$R_{\binom{s}{p}\pm}(z) = R_{\binom{s}{p}\pm}(\pm\frac{\ell_0}{2})e^{-2\kappa_0\left(\frac{\ell_0}{2}\mp z\right)}, \tag{10}$$

so in the product, the z dependence vanishes with

$$R_{\binom{s}{p}+}(z)R_{\binom{s}{p}-}(z) = R_{\binom{s}{p}+}(\frac{\ell_0}{2})R_{\binom{s}{p}-}(-\frac{\ell_0}{2})e^{-2\kappa_0\ell_0}, \tag{11}$$

giving $Д_{\binom{s}{p}}$ from (4) and F from (3) and (6) independent of z across the layer.

Solution z independence is evident across the middle layer in the multilayer solutions given in the literature. For a three-layer stack the jumps at $z = \pm\ell_0/2$ define the products of Fresnel reflection coefficients $R_{\binom{s}{p}+}R_{\binom{s}{p}-} = r_{\binom{s}{p}+}(\ell_0/2)r_{\binom{s}{p}-}(-\ell_0/2)\exp(-2\kappa_0\ell_0)$ from (8) and (9), which agrees with the Lifshitz formula (Eq. (4.14) in Dzyaloshinskii et al. [21], with some substitutions). For a five-layer stack $n_\ell = 2$ with layers of thicknesses ℓ_j counted by $-2 \le j \le 2$ as in Figure 3, we obtain products of Fresnel reflection coefficients as in (11) with the reflection coefficients $R_{\binom{s}{p}\pm}(\pm\ell_0/2)$ defined by (7) using the two upstream jump coefficients $r_{\binom{s}{p}\pm}(\pm(\ell_{\pm1} + \ell_0/2))$ defined in (8) and (9), which agrees with Zhou and Spruch (Eqs. (3.8) and (3.12)–(3.16) in [22]). The formulae give similar agreement for the Casimir force in (3) or (6) with any number of layers as developed in numerous studies [23, 24, 25].

3. Casimir Effect in a Graded-Permittivity Medium

The definition for the Casimir force from Eqs. (3) or (6) is applicable too in a graded-permittivity medium with a 1D continuous permittivity $\varepsilon(z)$, as can be seen by approximating the permittivity variation by discrete layers, for some small layer thickness Δz, as illustrated in Figure 4. A spatially shifted form of the recursion formula (7) lends itself directly to numerical computations for propagation of the Fresnel reflection coefficients far from the domain of interest with initial $R_{\binom{s}{p}\pm} = 0$ through intervals with centered permittivity jumps written for the left-sided coefficients

$$R_{\binom{s}{p}-}(z) = \frac{r_{\binom{s}{p}-}(z - \Delta z/2) + R_{\binom{s}{p}-}(z - \Delta z)e^{-\kappa(z-\Delta z)\Delta z}}{1 + r_{\binom{s}{p}-}(z - \Delta z/2)R_{\binom{s}{p}-}(z - \Delta z)e^{-\kappa(z-\Delta z)\Delta z}}e^{-\kappa(z)\Delta z}, \tag{12}$$

for jump coefficients $r_{\binom{s}{p}-}(z - \Delta z/2)$ still defined as in (8) and (9). The right-sided reflection coefficients $R_{\binom{s}{p}+}$ could be propagated similarly from $z \to \infty$ in the $-z$ direction, but in our numerical models they are defined using the relation $R_{\binom{s}{p}+}(z) = R_{\binom{s}{p}-}(-z)$ applicable to symmetric arrangements around a middle $z = 0$. A direct computational approach like this one has been applied to estimate the Casimir effect in linearly graded media by Inui [26].

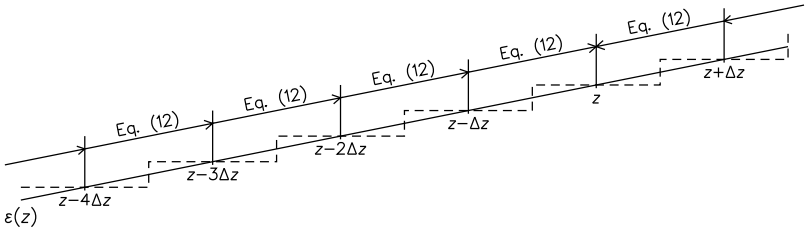

Figure 4. Direct calculation of Fresnel reflection coefficients in a graded-permittivity medium. A continuous permittivity variation $\varepsilon(z)$ is approximated by discrete layers of small thickness Δz.

The Fresnel recursion formula for a graded-index medium (7) or (12) with (8) and (9) is written in the limit that the interval Δz becomes infinitesimal $\Delta z \to 0$ by the differential equation for the continuous variation of the Fresnel reflection coefficients $R_{\binom{s}{p}\pm}(z)$, as in the example [20, Section 1.6]. Retaining only terms to first order in Δz, we obtain from either recursion relation

$$\frac{\partial R_{\binom{s}{p}-}}{\partial z} = r_{\binom{s}{p}-}(z)\left(1 - R_{\binom{s}{p}-}(z)^2\right) - 2\kappa(z)R_{\binom{s}{p}-}(z), \tag{13}$$

with the jump coefficients approximated by derivatives for the spatially continuously permittivity $\varepsilon(z)$

$$r_{s-}(z) = \frac{1}{2\kappa(z)}\frac{\partial \kappa}{\partial z} = \left(\frac{\xi}{2c\kappa(z)}\right)^2 \frac{\partial \varepsilon}{\partial z}, \tag{14}$$

$$r_{p-}(z) = \left(\frac{1}{2\kappa(z)}\frac{\partial \kappa}{\partial z} - \frac{1}{2\varepsilon(z)}\frac{\partial \varepsilon}{\partial z}\right) = \left(\left(\frac{\xi}{2c\kappa(z)}\right)^2 - \frac{1}{2\varepsilon(z)}\right)\frac{\partial \varepsilon}{\partial z}, \tag{15}$$

with the wavenumber $\kappa(z)$ still defined by Eq. (5); $\varepsilon(z)$ and $\kappa(z)$ retain their dependencies on the frequencies ξ and/or ϖ implicitly.

We examine bounded solutions with everywhere-small reflection coefficients $|R_{\binom{s}{p}-}(z)| \ll 1$, which is consistent with our main interest in small periodic permittivity fluctuations on top of a constant permittivity background. Thus we are able to linearize Eq. (13) and obtain the closed-form integral solution

$$R_{\binom{s}{p}-}(z) = e^{-2\int \kappa(z)dz}\left[\int e^{2\int \kappa(z)dz} r_{\binom{s}{p}-}(z)\left(1 - R'_{\binom{s}{p}-}(z)^2\right)dz\right]. \tag{16}$$

The function $R'_{\binom{s}{p}-}(z)$ represents a prior approximation to the Fresnel reflection coefficients, which we apply in our numerical iterations. For our analytic evaluation,

we leave the integrals all as indefinite and functions of z. A lower bound on the integral in the exponential integrating factor is of course arbitrary, as any constant in the exponential factors out of the main integral to cancel with the same constant from the outer exponential.

With an added constant of integration in the square brackets in (16), a term is added to the reflection coefficient due to the leading external exponential integrating factor, which diverges as $z \to -\infty$ for $R_{\binom{s}{p}-}(z)$ as $\kappa(z)$ is always positive, or as $z \to +\infty$ in the similar expression for $R_{\binom{s}{p}+}(z)$. Leaving the main integral in square brackets as indefinite always gives bounded solutions.

Bounded reflection coefficients must also be periodic with a periodic permittivity fluctuation, as shifting the origin of the calculation by any number of wavelengths $n\lambda$ in z cannot change the form of the solution. For a periodic permittivity fluctuation, the wavenumber from (5) can always be written as a constant plus a spatially periodic term $\kappa(z) = \tilde{\kappa}_0 + \tilde{\kappa}_1(z)$, giving an exponential integrating factor that decomposes into the product of constant and spatially periodic functions $\exp(2\int \kappa(z)dz) = \exp(2\tilde{\kappa}_0 z)\exp(2\int \tilde{\kappa}_1(z)dz)$, as the integral of a periodic function with zero average like $\tilde{\kappa}_1(z)$ is also periodic. Thus shifting the origin of the main indefinite integral in (16) by an integer number n of wavelengths $z \to z + n\lambda$, factors the constant $\exp(2n\tilde{\kappa}_0\lambda)$ out from the square brackets leaving the square brackets unchanged, and this constant just cancels with its inverse from the outer exponential. Even the perturbation term $R'_{\binom{s}{p}-}(z)$ defined by a previous iteration must be periodic, so periodic solutions generalize beyond the linear case with $R_{\binom{s}{p}-}(z) = R_{\binom{s}{p}-}(z + n\lambda)$.

Leaving the main integral as indefinite in (16) is convenient for our analytic evaluation, but in numerical implementations, the integral must be evaluated between specified limits. Then we include an added constant of integration in the square brackets, which we define by the periodicity condition $R_{\binom{s}{p}-}(z) = R_{\binom{s}{p}-}(z+\lambda)$ for arbitrary z for periodic permittivity variations. A computationally desirable form for the constant of integration for numerical applications is derived in Appendix B.

The Fourier decomposition for the spatial variation of a permittivity wave in z with minimum permittivity at $z = 0$ is written

$$\varepsilon(z) = \tilde{\varepsilon}_0 - \tilde{\varepsilon}_{1\mathrm{c}} \cos \frac{2\pi z}{\lambda}, \tag{17}$$

using the tilde $\tilde{\varepsilon}_{k(\mathrm{cs})}$ to denote the (real) spatial Fourier wave mode with wavenumber k in cosine (c) or sine (s) elements. The Fourier wave modes retain the Matsubara frequency ξ dependence implicitly $\tilde{\varepsilon}_0 = \tilde{\varepsilon}_0(\xi)$ and $\tilde{\varepsilon}_{1\mathrm{c}} = \tilde{\varepsilon}_{1\mathrm{c}}(\xi)$. We do not introduce temporal varying factors here as wave changes are always assumed to be slow compared to frequencies that are important for the Casimir effect. The permittivity variation $\varepsilon(z)$ might represent a standing wave like what is indicated in Figure 2, which does not change its spatial form but exhibits a sinusoidal temporal variation through an external temporal factor, as $\varepsilon(z) \to \varepsilon(z)\cos 2\pi\nu t$ or in the usual analytically continued form with $\varepsilon(z) \to \varepsilon(z)\exp(i2\pi\nu t)$ and $\cos(2\pi z/\lambda) \to \exp(i2\pi z/\lambda)$ as we employ

in spatial/temporal Fourier analyses in Section 6. Solutions for traveling waves are obtained similarly with a $\pm z$ moving wavefront by the replacement $z \to \lambda\nu t \mp z$.

Assuming a relatively small wave amplitude $|\tilde{\varepsilon}_{1c}| \ll |\tilde{\varepsilon}_0|$, the jump coefficients $r_{\binom{s}{p}-}(z)$ and the wavenumber $\kappa(z)$ are written to first order in $\tilde{\varepsilon}_{1c}$ using the z derivative of the permittivity from (14) and (15) and the definition (5)

$$r_{\binom{s}{p}-}(z) = \tilde{r}_{\binom{s}{p}1s} \sin\frac{2\pi z}{\lambda}, \tag{18}$$

$$\kappa(z) = \tilde{\kappa}_0 - \tilde{\kappa}_{1c} \cos\frac{2\pi z}{\lambda}, \tag{19}$$

where

$$\tilde{r}_{s1s} = \frac{\pi\xi^2\tilde{\varepsilon}_{1c}}{2c^2\lambda\tilde{\kappa}_0^2},\ \tilde{r}_{p1s} = \tilde{r}_{s1s} - \frac{\pi\tilde{\varepsilon}_{1c}}{\lambda\tilde{\varepsilon}_0},$$

$$\tilde{\kappa}_0 = \frac{1}{c}(\tilde{\varepsilon}_0\xi^2 + \varpi^2)^{1/2},\ \text{and}\ \tilde{\kappa}_{1c} = \frac{\xi^2\tilde{\varepsilon}_{1c}}{2c^2\tilde{\kappa}_0}.$$

Note that to first order, $\tilde{\kappa}_0$ is independent of $\tilde{\varepsilon}_{1c}$, and all of the other coefficients are proportional to $\tilde{\varepsilon}_{1c}$.

Substituting into (16) and retaining terms only to first-order in the permittivity fluctuation $\tilde{\varepsilon}_{1c}$, leaves the analytic integral for the Fresnel reflection coefficients

$$R_{\binom{s}{p}-}(z) = \tilde{r}_{\binom{s}{p}1s} e^{-2\tilde{\kappa}_0 z} \int e^{2\tilde{\kappa}_0 z} \sin\frac{2\pi z}{\lambda} dz = \frac{\tilde{r}_{\binom{s}{p}1s}}{2} \frac{\tilde{\kappa}_0 \sin\frac{2\pi z}{\lambda} - \frac{\pi}{\lambda}\cos\frac{2\pi z}{\lambda}}{\tilde{\kappa}_0^2 + \left(\frac{\pi}{\lambda}\right)^2}. \tag{20}$$

The indefinite form of the integral gives a periodic solution as we expect.

The Fresnel reflection coefficients $R_{\binom{s}{p}\pm}(z)$ make contributions to the Casimir force in (3) or (6) through their products $R_{\binom{s}{p}+}(z)R_{\binom{s}{p}-}(z)$. Remembering that $R_{\binom{s}{p}+}(z) = R_{\binom{s}{p}-}(-z)$ for a symmetric permittivity variation around $z = 0$ as in the wave from (17), we obtain

$$R_{\binom{s}{p}+}(z)R_{\binom{s}{p}-}(z) = \frac{\lambda^2}{8\pi^2}\tilde{r}^{\,2}_{\binom{s}{p}1s}\left(\frac{1}{\chi^2+1}\cos\frac{4\pi z}{\lambda} - \frac{\chi^2-1}{(\chi^2+1)^2}\right), \tag{21}$$

defining the new variable $\chi \equiv \tilde{\kappa}_0\lambda/\pi$.

The jump coefficient $\tilde{r}_{p1s}$ from (15) is of order and $\tilde{r}_{s1s}$ from (14) of order or smaller than the relative permittivity fluctuation $\tilde{\varepsilon}_{1c}/\tilde{\varepsilon}_0$, being possibly smaller since $\tilde{\kappa}_0^2 = \tilde{\varepsilon}_0\xi^2/c^2 + \varpi^2/c^2 \geq \tilde{\varepsilon}_0\xi^2/c^2$. Thus the product $R_{\binom{s}{p}+}(z)R_{\binom{s}{p}-}(z)$ is no larger than second order in the relative permittivity change. The offset in the denominator of $Д_{\binom{s}{p}}(z)$ in (4) introduces a still smaller-order effect, so for a small-amplitude standing permittivity wave, the Casimir force from Eq. (6) is written to most-significant order in the relative permittivity fluctuation as

$$F(z) = \frac{\pi\hbar}{2\lambda^3}\left(\int_0^\infty\int_0^\infty \chi^2 R_{s+}(z)R_{s-}(z)d\chi d\xi + \int_0^\infty\int_0^\infty \chi^2 R_{p+}(z)R_{p-}(z)d\chi d\xi\right), \tag{22}$$

having eliminated the variables κ_0 and ϖ by substituting with the new variable χ. The jump coefficients from (14) and (15) are written in terms of χ as

$$\tilde{r}_{s1s} = \frac{\xi^2\lambda\tilde{\varepsilon}_{1c}}{2\pi c^2\chi^2}, \quad \tilde{r}_{p1s} = \tilde{r}_{s1s} - \frac{\pi}{\lambda}\frac{\tilde{\varepsilon}_{1c}}{\tilde{\varepsilon}_0}. \tag{23}$$

The polarization product $R_{s+}(z)R_{s-}(z)$ goes like $1/\chi^6$ asymptotically for $\chi \gg 1$, which makes a $1/\chi^4$ contribution to the first integral in (22), whereas the second polarization product $R_{p+}(z)R_{p-}(z)$ goes like $1/\chi^2$ at large χ, so the second integral in (22) is linearly divergent. The second divergent p polarization integral is dominant, so we drop the integral over s polarizations in (22) and obtain

$$F(z) = \frac{\pi\hbar}{16\lambda^3}\left(\int_0^\infty \left(\frac{\tilde{\varepsilon}_{1c}}{\tilde{\varepsilon}_0}\right)^2 d\xi\right)\left(\cos\frac{4\pi z}{\lambda}\int_0^{\chi_c}\frac{\chi^2}{\chi^2+1}d\chi - \int_0^{\chi_c}\chi^2\frac{\chi^2-1}{(\chi^2+1)^2}d\chi\right), \quad (24)$$

having factored out the ξ integral with the permittivity contrast $\tilde{\varepsilon}_{1c}/\tilde{\varepsilon}_0$, supposing no dependence upon ξ in the cutoff χ_c. The χ integral cutoff is determined by a cutoff frequency ω_c that is much higher than the maximum frequency for permittivity fluctuations, which is the electronic vibration frequency, and so can be approximated $\chi_c \simeq \lambda\omega_c/(\pi c)$.

The divergent integral is treated by introducing a smooth Lorentzian cutoff function into integrations around an upper χ_c in our numerical calculations as a form of covariant regularization [27, Section 9.6][28, Section 9.2], and by simply truncated the integral at χ_c in this analytic derivation. Both procedures give very similar estimates for the Casimir force as we discuss in Section 5.

Regularization by imposing a maximum frequency cutoff natural to the physical process seems sufficient for our interest in estimating the amplitude and in exploring general properties of the Casimir effect in permittivity waves. We argue that electronic reactivity to virtual photons must be limited by a maximum recoil due to the small but finite electron inertia, or perhaps equivalently the qed calculation exhibits a small but finite correlation length represented by the Compton wavelength [29, Chapters 8-9]. In either case, the Compton frequency seems the only relevant choice for an upper frequency cutoff in ordinary materials, as is used in other studies that test the Casimir effect, and as has been successfully applied with other zp effects, historically and most famously with the Lamb shift [30], [28, Section 9.6.2]. Thus we take $\omega_c = m_e c^2/\hbar$=7.76E20 rad/s for m_e the electron mass.

The χ integrals in (24) are analytic and both well approximated by the value of their upper limits χ_c for $\chi_c \gg 1$, thus giving

$$F(z) = \frac{\hbar\omega_c}{16\lambda^2 c}\left(\int_0^\infty \left(\frac{\tilde{\varepsilon}_{1c}}{\tilde{\varepsilon}_0}\right)^2 d\xi\right)\left(\cos\frac{4\pi z}{\lambda} - 1\right). \quad (25)$$

The Casimir force in a medium with a small-amplitude relative permittivity fluctuation goes as $1/\lambda^2$ at all wavelengths, and is second-order in the relative permittivity fluctuation. The force exhibits significant power in its spatially constant and $\cos(4\pi z/\lambda)$ wave modes only, and ranges from zero, where cos = 1, to a maximum negative value where cos = −1. Thus the Casimir effect in small-amplitude permittivity waves is always repulsive. We refer to the Casimir modes separately equating terms in the spatial Fourier expansion $F(z) = \tilde{F}_0 + \tilde{F}_{2c}\cos 4\pi z/\lambda$.

This largest-amplitude spatial wave mode contributing to the Casimir force from (25) does not change sign with the changing sign of the permittivity wave, as the

permittivity contrast enters only with its squared value. The Casimir force vanishes when the wave permittivity contrast vanishes at zero temporal phase, and so the Casimir force is modulated with twice the permittivity wave frequency 2ν. It can be seen that spatial wave modes other than $\cos(4\pi z/\lambda)$ exhibit terms proportional to $\tilde{r}_{\binom{s}{p}1\mathrm{s}}$ and so do exhibit variations at the normal wave frequency ν, but these terms are of lesser order in powers of the relative permittivity fluctuation. We study the properties of the smaller-order Casimir wave modes numerically in Section 5.

4. Casimir Effect in an Alternating-Layer Stack

Figure 5 illustrates the Casimir force in the middle layer of an alternating-layer stack as a function of the spatial scale $\lambda = \ell_- + \ell_+$ for permittivities $\varepsilon_\pm(\xi)$ as in the drawing Figure 1 or from Figure 3 with equal layer thicknesses $\ell_+ = \ell_-$. The three-layer calculation ($n_\ell = 1$) derived by integrating numerically Eq. (6) is shown with three-layer calculations for three temperatures using the Matsubara sum from (3) (*solid lines*), with the 41-layer calculation ($n_\ell = 20$) with (6) (*dot dot long-dash*), and with limiting power-law forms $F_\langle$ (*dot dash*) and $F_\rangle$ (*long dash*) from Eqs. (A.3) and (A.6), respectively, discussed in Appendix A. The lower panel illustrates the same data on an expanded scale with the 3-layer curve subtracted.

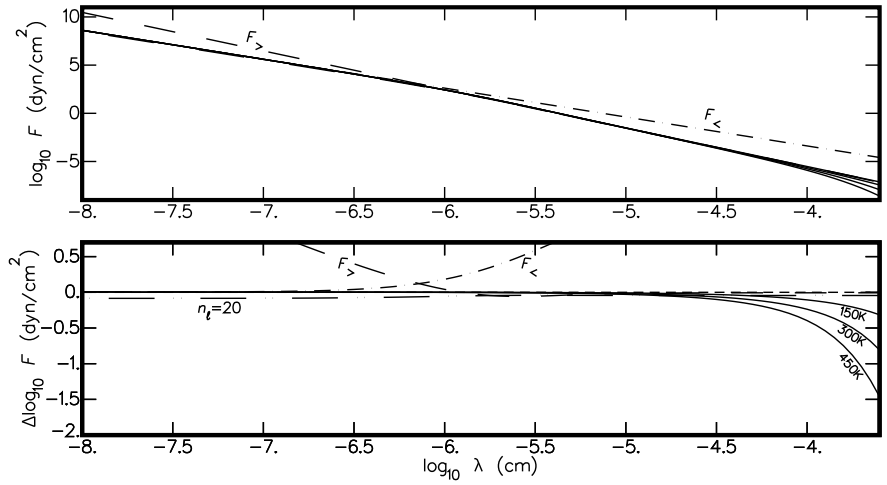

Figure 5. Casimir force as a function of scale $\lambda = \ell_- + \ell_+$, from 1E−8 cm=1Å to 1E−3.6 cm=2.5μm, with alternating static-permittivity contrast $\Delta\varepsilon_\mathrm{e}/\varepsilon_\mathrm{e} = 0.01$, for 3 layers and for three temperatures (*solid lines*), for 41 layers $n_\ell = 20$ (*dot dot long-dash*), compared with limiting power laws $F_\langle$ (*dot dash*) and $F_\rangle$ (*long dash*). The same data are shown in the lower panel on an expanded vertical scale with $\log_{10} F$ for 3 layers subtracted.

For our models, we adopt a usual form for the complex permittivity as a function of light frequency ξ

$$\hat{\varepsilon}(\xi) = 1 + \frac{\varepsilon_\mathrm{e} - 1}{1 - \xi^2/\omega_\mathrm{e}^2} - \frac{\omega_\mathrm{p}^2}{\xi(\xi + i\gamma_\mathrm{p})}, \tag{26}$$

which is defined by a single electronic band at frequency ω_e characteristically ∼2E16 rad/s of strength $\varepsilon_e - 1$, and a conductive term defined by the plasma frequency ω_p, which ranges from 0 to 2E15 rad/s in semiconductors, and reaches about 1.6E16 rad/s in doped semiconductors or in the best room-temperature metallic conductors, with the Drude collision frequency γ_p, characteristically ∼2E14 rad/s. The simplified form contains the important terms for the Casimir effect [17]. A lattice vibration band at lower frequency (typically 9E12 rad/s) represents the next lower frequency effect in crystals, but is both below the important frequency range and of relatively small oscillator strength to make a significant contribution to the Casimir effect. The main contribution to the static permittivity comes from the electronic vibration band with $\hat{\varepsilon}(\xi = 0) = \varepsilon_e$; ε_e ∼6 for materials of interest.

Due to causal restrictions, models for the complex permittivity must always be real on its imaginary frequency axis. The real projected permittivity from (26) is defined $\varepsilon(\xi) \equiv \hat{\varepsilon}(i\xi)$, which gives

$$\varepsilon(\xi) = 1 + \frac{\varepsilon_e - 1}{1 + \xi^2/\omega_e^2} + \frac{\omega_p^2}{\xi(\xi + \gamma_p)}. \tag{27}$$

The projected permittivity $\varepsilon(\xi)$ must be a slowly varying monotonically decreasing function [17], and is plotted in many places for conductors or nonconductors (e.g. see Figure 20 [11]). For the calculations for Figure 5, the material is assumed to be nonconductive ($\omega_p = 0$), with ω_e=2E16 rad/s and ε_e=6, with static permittivities ε_{ej} in successive layers j alternating between $\varepsilon_{e\pm} = \varepsilon_e \pm \Delta\varepsilon_e$; for the figure the permittivity contrast used was $\Delta\varepsilon_e/\varepsilon_e$=0.01. Following the convention used in earlier sections, the middle $j = 0$ and even j layers are denoted by the subscript '−' and the odd j layers by '+'. Though the formulation discussed is mostly applicable to arbitrary multilayer stacks with numbered layers, we remain interested primarily in stacks of alternating ± layers.

For small permittivity changes $|\Delta\varepsilon| \ll \varepsilon$, the parametric representation in the model (26) and (27) is assumed to remain accurate. Then the permittivity change can be described by the derivative expansion

$$\Delta\varepsilon = \frac{\partial\varepsilon}{\partial\varepsilon_e}\Delta\varepsilon_e + \frac{\partial\varepsilon}{\partial\omega_e}\Delta\omega_e + \frac{\partial\varepsilon}{\partial\omega_p}\Delta\omega_p + \frac{\partial\varepsilon}{\partial\gamma_p}\Delta\gamma_p. \tag{28}$$

Physical processes in materials change permittivity parameters in different ways, so we explore the Casimir effect with different changing parameters in our numerical models. Although such parametric processes should give the most-significant contribution to the Casimir effect that can be introduced with acoustic waves, additional spectral effects not represented in the permittivity model of (26) also enter. The permittivity spectrum $\varepsilon(\xi)$ exhibits significant changes with pressure in the vicinity of lattice vibration resonances commonly described as a spectral variations in the photoelastic coefficient [31, Chapter 9]. The photoelastic coefficient enters in the phenomenological acoustic wave theory, which we describe at the beginning of Section 8. We note in our numerical experiments the very different limiting forms that arise when different parameters controlling the permittivity are perturbed.

As is well-known and evident in Figure 5, the Casimir force for a three-layer stack exhibits relatively small- and large-scale limiting power-law forms. Our Figure 5 in the 41-layer $n_\ell = 20$ calculation (*dot dot long-dash*) suggests the generalization of this property to arbitrary multilayer stacks. As long as the jump coefficients for a multilayer stack are small $|r_{\binom{s}{p}\pm}| \ll 1$, their contribution to the reflection coefficients $R_{\binom{s}{p}\pm}$ in (7) are increasingly exponentially attenuated with increasing distance from the middle $z = 0$. The final exponential factor in the recursion formula $\exp(-2\kappa(0)\ell_0)$ as it appears in (11), must always be the dominant one, and increasing the number of layers cannot much change the limiting form of the integral. We reexamine and explore the scope of the Lifshitz limiting solution forms in Appendix A.

We find it convenient to use the spatial period in alternating layers as the relevant scale, i.e. the wavelength $\lambda = \ell_- + \ell_+$. Though the thickness of the middle layer ℓ_- alone would be the natural choice, the full period facilitates comparison with the wavelength for the Casimir effect in graded media described in subsequent sections. Though we use wavelength for the dependent variable, and assume equal odd-even layer thicknesses in all the figures shown in this section with $\lambda = \ell_- + \ell_+ = 2\ell_-$, the Casimir effect in an alternating-layer stack is essentially determined by the even layer thickness ℓ_- alone, and changes little with changes in the relative thickness of the odd layers ℓ_+/ℓ_- over several orders of magnitude.

In our numerical calculations, the infinite-frequency integrals in ξ and ϖ in Eqs. (3) and (6) are written as finite angular integrals by substituting for each ξ or ϖ with $\omega_\mathrm{e} \tan^\iota \theta$ and integrating from $\theta = 0$ to $\pi/2$. The ξ integral is convergent because the permittivity goes to zero for $\xi \gg \omega_\mathrm{e}$. Though the ϖ integral is divergent in general, an effect evident for graded media as we have discussed, it is convergent for multilayer stacks due to exponential attenuation of reflection coefficients from (11), which cuts off at wavenumbers $\kappa(0) \gg 1/\ell_0$ in the middle layer or frequencies $\varpi \gg \kappa(0)c = c/\ell_0$. We find that the integrals converge consistently in the fewest integration steps with the power $\iota = 6$, and obtain relative accuracies better than 1E−3 using Simpson's rule with 120 steps, which is what we used for all the multilayer calculations described here.

Figure 6 shows the Casimir force $F(\lambda)$ for alternating static permittivity ε_e in (a), electronic vibration frequency ω_e in (b), and plasma frequency ω_p in (c). The static permittivity (a) and the electronic frequency (b) alternate with the small differences identified in the figure, but the plasma frequency (c) alternates between $\omega_\mathrm{p} = 0$ in the nonconducting even layers and $\omega_{\mathrm{p}+}$ in conducting odd layers with γ_p=2E14 rad/s. Results are overplotted for calculations made with increasing numbers of layers $n_\ell = 1$, 2, 3, 5, ... (all shown as *dashed*), and $n_\ell = 20$ (*solid*). Relative changes less than 5E−3 in the estimated Casimir force over the range of scales are found with increasing the number of layers used in the calculation above about $n_\ell = 3$.

The Casimir force estimates all follow the $1/\lambda^3$ or $1/\ell_0^3$ thin-limit power-law form, but the thick-limit power law $1/\ell_0^4$ does not apply with fluctuations of the electronic vibration frequency $\Delta\omega_\mathrm{e}/\omega_\mathrm{e}$ as we elaborate in Appendix A. The numerical experiments for the fluctuating electronic vibration frequency ω_e (b) suggest another definite thick-

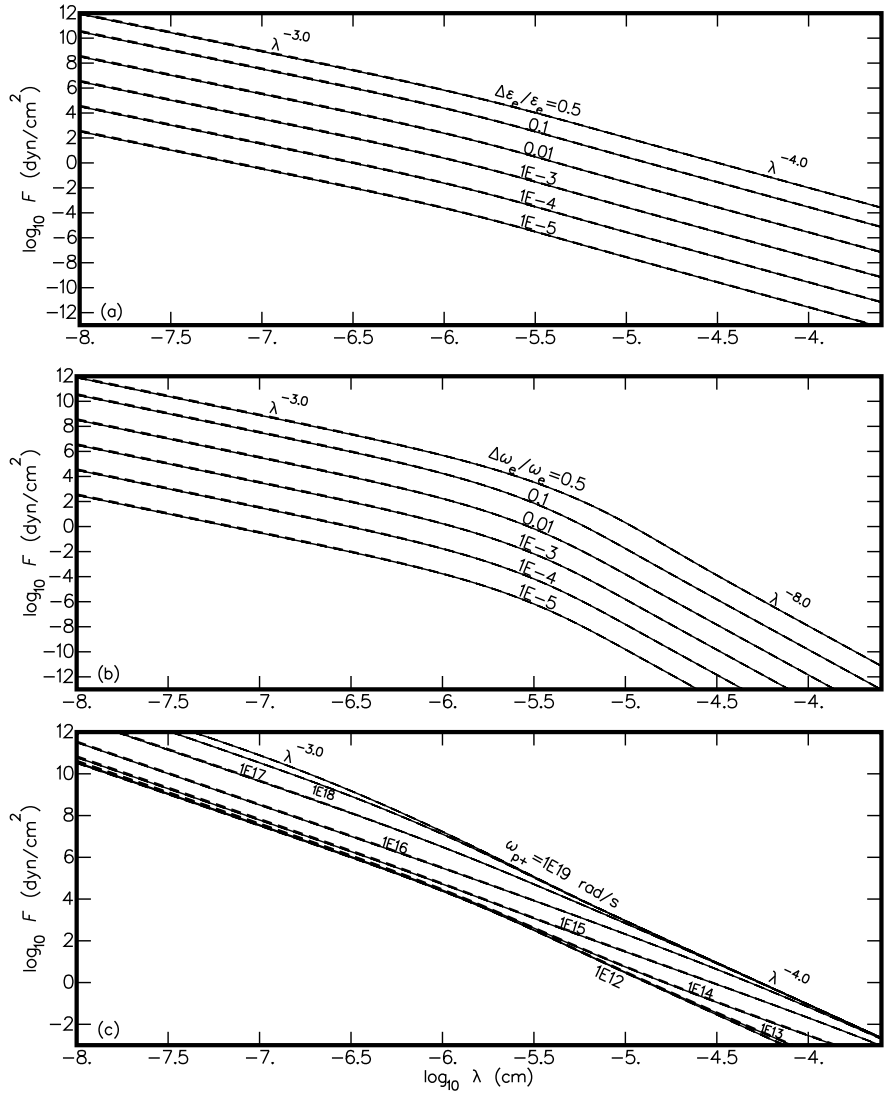

Figure 6. Casimir force $F(\lambda = \ell_- + ell_+ = \ell_-/2)$ in the central layer of a multilayer stack with alternating static permittivity ε_e (a), alternating electronic vibration frequency ω_e (b), and plasma frequency in the odd layers $\omega_{\mathrm{p}+}$ (c). Calculations with different parameter contrasts for 41 layers n_ℓ = 20 (*solid*) and fewer n_ℓ=1, 2, 3, 5, ... (*dashed*) are shown.

layer power-law form of $1/\ell_0^8$. Though power-law dependencies $1/\ell_0^3$ and $1/\ell_0^4$ are seen over ranges in λ or ℓ_0 with alternating plasma frequency in panel (c), these do not show a single cross-over separation, but effects depend strongly and specifically upon the plasma frequency contrast.

The separation between the successive force curves with increasing permittivity contrast goes as the relative contrast squared, $(\Delta\varepsilon_\mathrm{e}/\varepsilon_\mathrm{e})^2$ in panel (a), and as $(\Delta\omega_\mathrm{e}/\omega_\mathrm{e})^2$ in (b), with deviations in the Casimir force across the range in λ no larger than 5E−3 up to relative contrasts 0.01. For higher contrasts, larger variations arise as nonlinear effects begin to be important. A squared dependence is natural, as the Casimir force

from (6) goes like $R^2_{\binom{s}{p}\pm}$. The reflection coefficients feel their main contribution from the first jump, and so must go like $R_{\binom{s}{p}\pm}(\ell_0/2) \sim r_{\binom{s}{p}\pm}$ as in the discussion following (11), and the jump coefficients follow the relative derivative $r_{\binom{s}{p}\pm} \sim (\partial\epsilon/\partial z)/\epsilon$ in their most significant contributions to the integrals, as might be seen from (14) and (15).

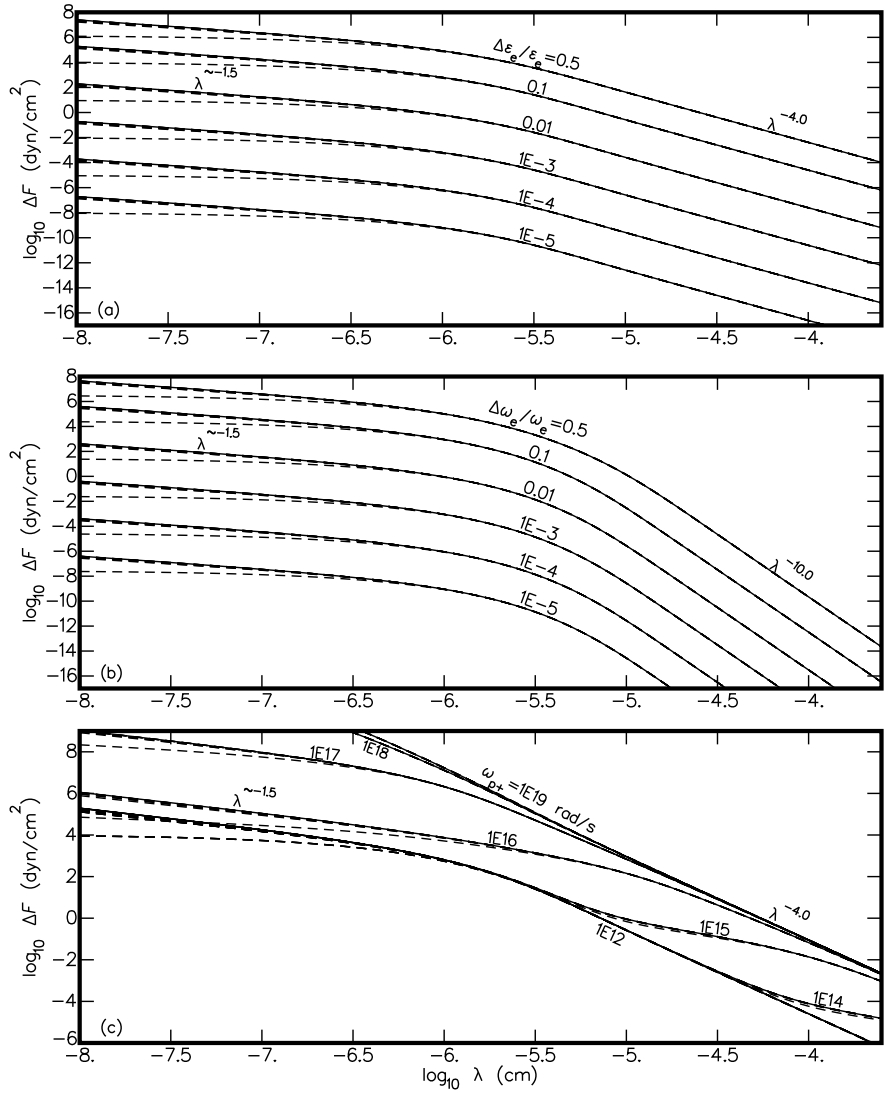

Figure 7. Casimir force difference $\Delta F(\lambda)$ between normal and permittivity-reversed stacks for alternating static permittivity $\varepsilon_{\rm e}$ (a), alternating electronic vibration frequency $\omega_{\rm e}$ (b), and plasma frequency in odd layers $\omega_{\rm p+}$ (c). Calculations with different parameter contrasts for 41 layers $n_\ell = 20$ (*solid*) and fewer n_ℓ=1, 2, 3, 5, ... (*dashed*) are shown.

Though the Casimir effect is mainly unchanged between the normal and the odd-even reversed stacks, small residual systematic differences do exist. The change in Casimir force between normal and reversed static-permittivity states $\Delta F(\lambda)$ is shown in Figure 7 for alternating static permittivities $\varepsilon_{\rm e}$ in panel (a), alternating electronic vibration frequency $\omega_{\rm e}$ in (b), and plasma frequency in odd layers $\omega_{\rm p+}$ in (c). Force

differences have to be computed before frequency integrals in (6) to avoid a large relative numerical noise, as the difference is small compared to the force itself. Force differences are overplotted for increasing numbers of adjacent layers used in the calculation $n_\ell = 1$, 2, 3, 5, ... (all shown as *dashed*), and $n_\ell = 20$ (*solid*). Relative changes no larger than about 0.05 are found for calculations made with more than about 7 layers ($n_\ell = 3$). Force differences between normal and reversed stacks $\Delta F(\lambda)$ increase as the permittivity contrast cubed in (a) and (b), as is natural for small differences between forces that are the same to second order in their even and odd permittivity contrasts.

Force differences exhibit good thick-layer power-law forms with fluctuating static permittivity ε_e following the same power law as what is seen as for the Casimir force $1/\ell_0^4$ in (a), and a much steeper thick-layer power-law form $1/\ell_0^{10}$ for fluctuating electronic frequency ω_e in (b). Force differences between a normal and reversed plasma-frequency change in (c) show characteristic power-law forms $1/\ell_0^3$ and $1/\ell_0^4$ over ranges in scale, but with no obvious dependence of the cross-over separation upon the plasma frequency contrast. Force differences do not exhibit very well-defined thin-layer power-law forms, but go only approximately as $1/\ell_0^{1.5}$ in all panels (a)–(c).

As the modulation of the Casimir force cycles between the nearly identical normal and reversed permittivity states it passes through zero, so with a permittivity modulation at frequency ν, the Casimir force is modulated mainly at the frequency 2ν.

5. Casimir Effect in a Permittivity Wave

Figure 8 shows an example Casimir force profile $F(z)$ over one wavelength in permittivity $\varepsilon(z)$ (illustrated on top), for λ=E−6.5 cm = 3.16 nm and contrast $\Delta\varepsilon_\mathrm{e}/\varepsilon_\mathrm{e} = 0.1$. The Casimir force profile (*upper panel*) is everywhere repulsive and ranges from zero for no effect at the permittivity wave maxima and minima to a maximum effect in the most slopping portions of the wave. Though most of the power is in the $\lambda/2$ wave $\tilde{F}_{2\mathrm{c}}$ and bulk $\tilde{F}_0$ modes, as expected from our analytic derivation in Section 3, a small residual remains, which is evident when the main Casimir wave modes are subtacted (*middle panel*). The residual mainly contains just the $\tilde{F}_{1\mathrm{c}}$ and $\tilde{F}_{3\mathrm{c}}$ modes. The Casimir force difference between normal and sign-reversed permittivity waves (*bottom panel*) closely follows the residual in the middle panel, showing twice its amplitude with matching relative $\tilde{F}_{1\mathrm{c}}$ and $\tilde{F}_{3\mathrm{c}}$ mode profiles. The main Fourier modes $\tilde{F}_0$ and $\tilde{F}_{2\mathrm{c}}$ do not change with the reversal of the permittivity wave phase and so vanish in the ΔF profile, however both of the other significant wave modes do fully. Thus the principle Fourier modes $\tilde{F}_0$ and $\tilde{F}_{2\mathrm{c}}$ are modulated with twice the frequency of the permittivity wave as we anticipated in Section 3, and the two residual modes $\tilde{F}_{1\mathrm{c}}$ and $\tilde{F}_{3\mathrm{c}}$ are modulated with the same frequency as the permittivity wave.

All of the Casimir force profiles for small amplitude permittivity waves $\Delta\varepsilon_\mathrm{e}/\varepsilon_\mathrm{e} \lesssim 0.1$ look qualitatively alike, being dominated by Casimir wave modes $\tilde{F}_0$ and $\tilde{F}_{2\mathrm{c}}$. However the Casimir force profile at large permittivity contrasts does noticeable change its appearance as illustrated in Figure 9, showing an increased contribution from secondary

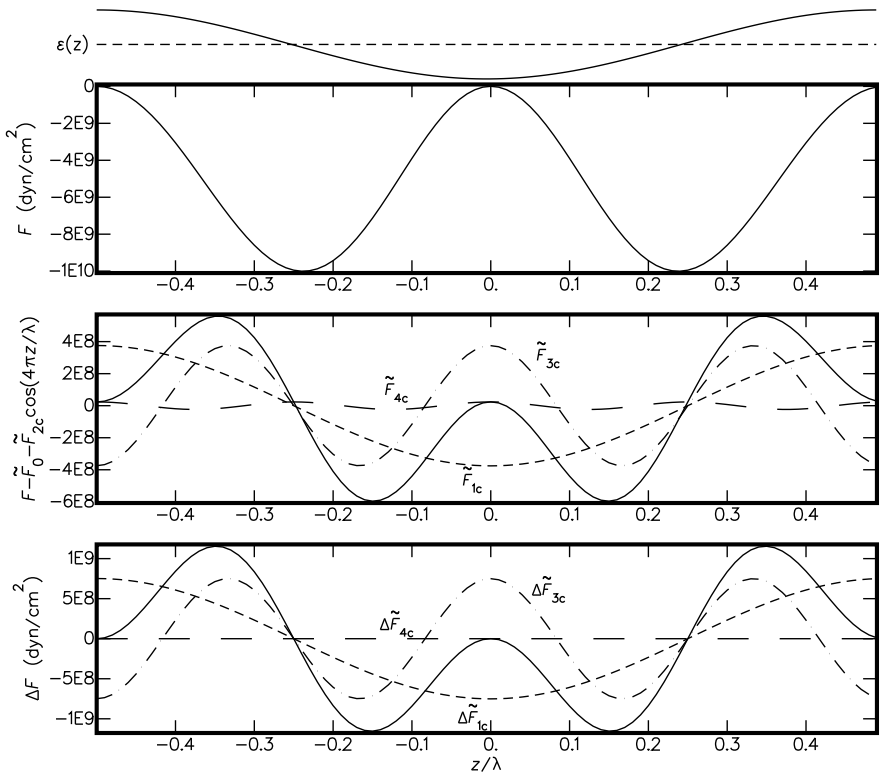

Figure 8. Casimir force profile $F(z)$ for λ=1E−6.5 cm= 3.16 nm (*upper panel*), with principle wave modes $\tilde{F}_0$ and $\tilde{F}_{2c}$ subtracted (*middle panel*), and the force difference $\Delta F(z)$ between the normal and reversed permittivity waves (*bottom panel*), showing decomposition of profiles into wave modes $\tilde{F}_{1c}$ (*dashed*), $\tilde{F}_{3c}$ (*dot dash*), and secondary residual $\tilde{F}_{4c}$ (*long dash*), for a permittivity wave of contrast $\Delta\varepsilon_e/\varepsilon_e = 0.1$ (illustrated on top), with ω_e=2E16 rad/s and ε_e=6.

Casimir wave modes $\tilde{F}_{1c}$ and $\tilde{F}_{3c}$, and a small but here significant contribution from $\tilde{F}_{4c}$ (*long dash*). For larger amplitude permittivity waves, profiles of the residual force (*middle panel*), and force difference (*lower panel*) differ noticeably, indicating that the secondary wave mode $\tilde{F}_{4c}$ oscillates at twice the frequency of the permittivity wave with the principle wave modes $\tilde{F}_0$ and $\tilde{F}_{2c}$.

For our numerical calculations the infinite integrals from (6) are evaluated as finite angular integrals as for the multielement stacks in Section 4 with sampling at 100 evenly spaced angular intervals. Integrals in ξ become negligible above the electronic vibration frequency ω_e and are cut off with a smooth function around $100\omega_e$. For general graded media, the integral in frequency ϖ is divergent, and so is smoothly truncated around the Compton frequency using a smooth Lorentzian, as we have described.

Reflection coefficients at each ξ and ϖ were derived in two ways, using the recursion relation Eq. (12) starting many wavelengths from the domain of interest, and using the integral method from (16). For self-consistent results within a percent, each method requires many samples per unit of the dissipative length scale $1/\tilde{\kappa}_0$, 100 samples with the recursion relation (12), and 10 with the integral method (16) using Simpson's rule.

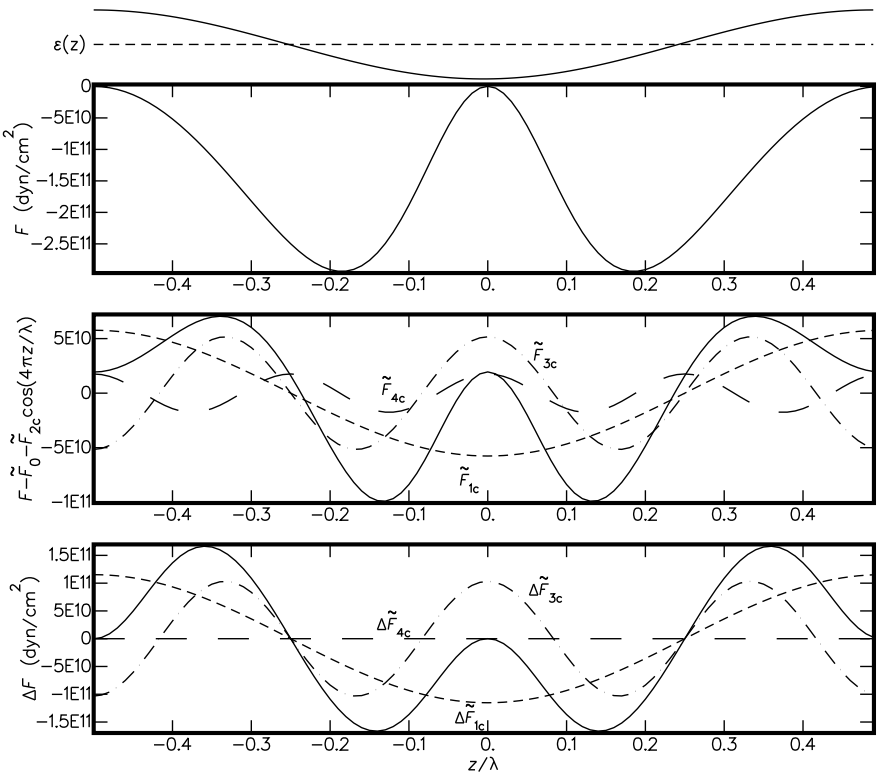

Figure 9. Casimir force profiles as in Figure 8 for a larger amplitude permittivity wave $\Delta\varepsilon_\mathrm{e}/\varepsilon_\mathrm{e} = 0.5$.

For the longest wavelength tested λ=1E−4 cm at the highest frequency ϖ=1E20 rad/s for wavenumber $\tilde{\kappa}_0 = \varpi/c$, $100\tilde{\kappa}_0\lambda$=3.3E7 recursion samples are needed or $10\tilde{\kappa}_0\lambda$=3.2E6 integration samples per wavelength. The integral method was iterated three times in the reflection coefficients $R_{\binom{s}{p}-}(z)$, and always gave good convergence showing changes no larger than 10% after the initial iteration.

Both methods give nearly identical results, except that the recursion method is noisier, with noise comparable to signal for a relative permittivity fluctuation of about 1E−4. The integral solution gives consistent solutions even for relative permittivity fluctuations as small as 1E−8. The figures shown here were obtained using the integral method.

The strength of the Casimir effect for a fluctuating static permittivity is approximated using (25) evaluating the integral with the permittivity model (27) for a nonconductor $\omega_\mathrm{p} = 0$ and estimating the wave contrast by the derivative $\tilde{\varepsilon}_{1\mathrm{c}}/\tilde{\varepsilon}_0 = \Delta\varepsilon/\varepsilon$ with $\Delta\varepsilon = (\partial\varepsilon/\partial\varepsilon_\mathrm{e})\Delta\varepsilon_\mathrm{e}$, which gives an analytic integral that is evaluated as

$$F(z) = \frac{\pi\hbar\omega_\mathrm{e}\omega_\mathrm{c}\varepsilon_\mathrm{e}^{1/2}}{64\lambda^2 c}\left(\frac{\Delta\varepsilon_\mathrm{e}}{\varepsilon_\mathrm{e}}\right)^2\left(\cos\frac{4\pi z}{\lambda} - 1\right). \tag{29}$$

For the parameters used in the Figure 8, the force has its most negative value for cos = −1 of F = −1.31E10 dyn/cm^2, a little larger than the most negative value for the numerical integrations from the figure. The small discrepancy arises because the

frequency cutoff in the numerical integrations is approximated by a smooth function rather than the sharp cutoff used in the analytic integral from (29).

Figure 10 shows the Casimir wave modes $\tilde{F}_{kc}(\lambda)$ (*upper panel*) and wave modes in the force difference $\Delta\tilde{F}_{kc}(\lambda)$ (*lower panel*) as functions of wavelength λ for a number of static-permittivity contrasts $\Delta\varepsilon_e/\varepsilon_e$= E−0.3, E−1, E−2, E−3, E−4, and E−5. Each of the wave modes follows the $1/\lambda^2$ power law predicted in Section 3.

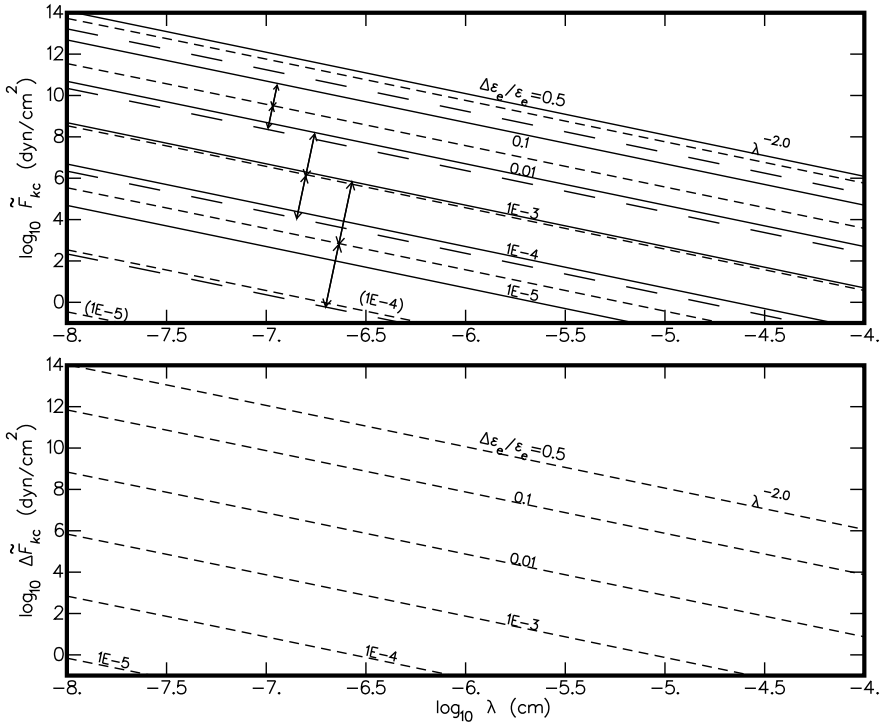

Figure 10. Casimir wave modes for the force $\tilde{F}_{kc}(\lambda)$ (*upper panel*) and the force difference $\Delta\tilde{F}_{kc}(\lambda)$ (*lower panel*) as functions of wavelength λ for different static-permittivity fluctuations $\Delta\varepsilon_e/\varepsilon_e$ showing the principle wave modes $\tilde{F}_0$ and $\tilde{F}_{2c}$ (everywhere coincident *solid*), residuals $\tilde{F}_{1c}$ and $\tilde{F}_{3c}$ (coincident *dashed*), and $\tilde{F}_{4c}$ (*long dash*). As wave modes overlap considerably, vectors are drawn to connect the successive $\tilde{F}_0$ with $\tilde{F}_{1c}$ and $\tilde{F}_{1c}$ with $\tilde{F}_{4c}$ in each permittivity contrast group. Only $\tilde{F}_{1c}$ and $\tilde{F}_{3c}$ appear in the force difference.

For the Casimir force (*upper panel*), the principle wave modes $\tilde{F}_{2c}$ (*solid*) are separated by two orders $2\log_{10}(\Delta\varepsilon/\varepsilon)$, so its amplitude goes like the permittivity contrast squared. The residual wave modes $\tilde{F}_{1c}$ (*dash*) and $\tilde{F}_{3c}$ (*dot dash*) always exhibit the same power and are exactly one order $\log_{10}(\Delta\varepsilon/\varepsilon)$ below the principle $\tilde{F}_{2c}$ (*solid*) in each permittivity contrast group. The Casimir wave mode $\tilde{F}_{4c}$ (*long dash*) is also consistently reproduced, but everywhere two orders $2\log_{10}(\Delta\varepsilon/\varepsilon)$ below the main component in each permittivity contrast group. In every case, the bulk mode $\tilde{F}_0$ follows exactly the wave mode $\tilde{F}_{2c}$. In the difference spectra (*lower panel*) the principle Casimir wave mode $\tilde{F}_{2c}$ and residual $\tilde{F}_{4c}$ disappear entirely. The difference spectra are composed of only the residuals $\tilde{F}_{1c}$ (*dash*) and $\tilde{F}_{3c}$ (*dot dash*), which exactly overlap and are

separated by two orders of permittivity contrast between groups.

Comparing the vertical scales between Figures 6 to 10 shows that the Casimir force for a sinusoidal wave of small wavelength scale λ=1E−7 cm=1 nm is almost a 1000 times larger than what is found for the equivalent square permittivity wave or multilayer stack. The relative sinusoidal-wave strength grows considerably larger too at larger wavelength since the Casimir force for for sinusoidal waves goes only as λ^{-2} whereas for square waves or multilayer stacks drops off as λ^{-3} or λ^{-4}.

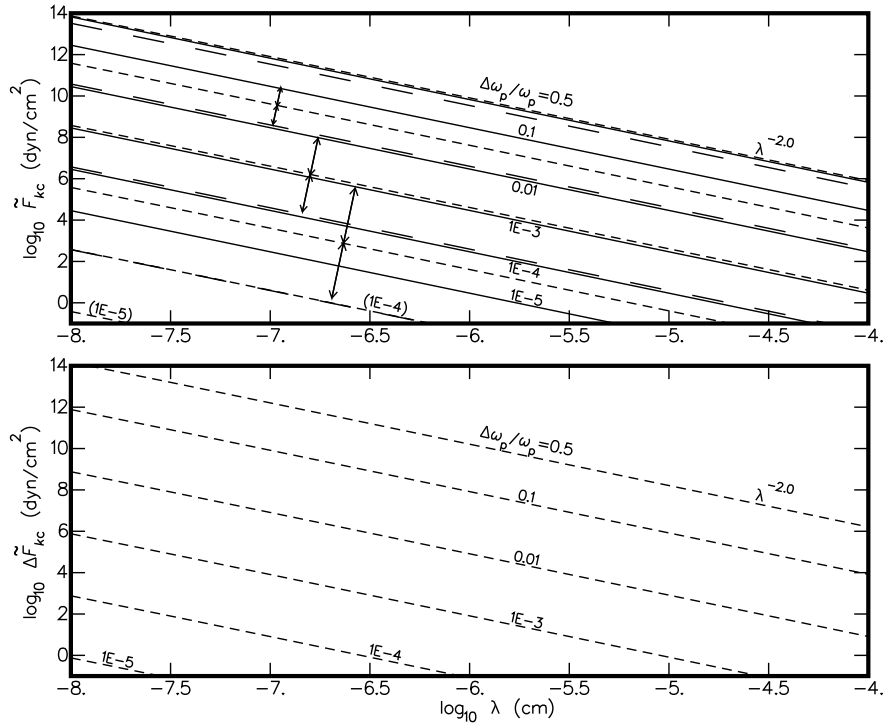

Figure 11. Casimir wave modes for the force $\tilde{F}_{kc}(\lambda)$ (*upper panel*) and the force difference $\Delta\tilde{F}_{kc}(\lambda)$ (*lower panel*) as functions of wavelength λ for different plasma frequency fluctuations $\Delta\omega_p/\omega_p$ identifying wave modes as in Figure 10. A plasma frequency of ω_p=1.6E16 rad/s was used characteristic of the best normal conductors.

Almost identical results are obtained with permittivity variations due to fluctuations in the electronic vibration frequency ω_e, so these are not shown. That solution is approximated from (25) with $\Delta\varepsilon = (\partial\varepsilon/\partial\omega_e)\Delta\omega_e$, giving

$$F(z) = \frac{\pi\hbar\omega_e\omega_c}{16\lambda^2 c}\frac{(\varepsilon_e-1)^2}{(\varepsilon_e^{1/2}+1)^3}\left(\frac{\Delta\omega_e}{\omega_e}\right)^2\left(\cos\frac{4\pi z}{\lambda}-1\right). \tag{30}$$

Equating the force amplitude with that of (29) with the same relative permittivity contrasts $\Delta\varepsilon_e/\varepsilon_e = \Delta\omega_e/\omega_e$, and solving numerically the transcendental equation shows that the forces are equal when ε_e=6.038948 , very close to the static permittivity we use in our models. A slightly larger Casimir force is obtained with static permittivity fluctuations in materials of lower static permittivity, and with fluctuations in electronic vibration frequency in materials of higher static permittivity.

Casimir profiles for a fluctuating plasma frequency or Drude collision frequency resemble the profiles shown in Figures 8 and 9, except that the sign of the fluctuations is reversed for fluctuations in the Drude collision frequency. Figure 11 shows the Casimir mode amplitude as a function of acoustic wavelength for a fluctuating plasma frequency with plasma frequency $\omega_{\rm p}$=1.6E16 rad/s and Drude collision frequency $\gamma_{\rm p}$=1E14 rad/s for good normal conductors (with $\varepsilon_{\rm e}$=6 and $\omega_{\rm e}$=2E12 rad/s). The Casimir wave modes $\tilde{F}_{1\rm c}$ and $\tilde{F}_{3\rm c}$ (*dashed*) here actually slightly exceed the principle modes $\tilde{F}_0$ and $\tilde{F}_{2\rm c}$ (*solid*) in the largest amplitude wave. The amplitude of the Casimir effect for plasma frequency fluctuations is proportional to the plasma frequency, and is little affected by changes in the other parameters.

Similar numerical tests made using the Matsubara sum from (3) in place of the integral from (6), with reflection coefficients derived using the integral method (16), show no temperature effect in the Casimir force in permittivity waves, having tested with contrasts up to $\Delta\varepsilon/\varepsilon$=0.5 and out to wavelengths as long as λ =E−3.5 cm=3.16 μm. We see no temperature effect whatsoever, perturbing any of the four parameters that enter the permittivity model (26).

6. Piezo ZP Energy Dynamics

The practical utilization of zp energy requires that the Casimir-induced variations in a crystal couple effectively to an external electrical load. In this section we consider the piezo effect for the Casimir wave solutions from Eq. (25) from Section 3 in both traveling and standing waves. The general energy transfer is described by assuming the conservation of an internal energy U (equivalent to the Gibbs free energy) in a stressed piezo crystal [32]

$$dU = T_{ij}dS_{ij} + E_i dD_i, \tag{31}$$

using the summation rule over repeated indices in a term, with the usual stress T_{ij} and strain S_{ij} 3×3 symmetric tensors containing both longitudinal and sheared components, and the electric field E_i and electric displacement D_i 3-element spatial vectors. Indices count coordinates $i = x, y, z$; x_i is the spatial coordinate $(x_1, x_2, x_3) = (x, y, z)$. For nonpyroelectric or magnetically affected piezo crystals and crystals that do not experience changes of state in the relevant ranges, the internal energy must be constant $dU = 0$, and the Casimir-forced internal stress couples exclusively to the crystal capacitance, so the total mechanical work $T_{ij}dS_{ij}$ over one wave cycle must balance the capacitive energy gain $-E_i dD_i$.

Material parameters are taken to be linearly coupled connected by two constitutive relations [32]. We choose the most convenient pair for this work [33]

$$T_{ij} = c^D_{ijk\ell}S_{k\ell} - h_{kij}D_k, \tag{32}$$

$$E_i = -h_{ijk}S_{jk} + \beta^S_{ij}D_j, \tag{33}$$

with the constant impermittivity at constant stress β^S_{ij} a 3×3 real matrix, which is the inverse of the unperturbed permittivity matrix ε_{ij} for low frequencies where the electric

fields are important in the generation of capacitances that drive external currents. The elastic stiffness $c_{ijk\ell}$ is a $3 \times 3 \times 3 \times 3$ real tensor, which is the inverse of the elastic compliance tensor $s_{ijk\ell}$, $c_{ijpq}s_{pqk\ell} = \delta_{(ij)}\delta_{(k\ell)}$, for the Kronecker delta $\delta_{(ij)}$. The piezoelectric constant h_{ijk} is a $3 \times 3 \times 3$ real tensor, which enters symmetrically between the material response for the inverse piezo effect in (32) and in the voltage response for the normal piezo effect in (33).

Stress-caused energetic processes do not give a capacitive transfer when the mechanical work done $T_{ij}dS_{ij}$ over a cycle vanishes. In such cases the stress T_{ij} and strain S_{ij} vary in phase. Then the electric displacement D_i and electric field E_i must also vary in phase for conservation of the total energy U from (31) and for consistency with the constitutive relations (32) and (33). Such zp energetics are conservative, so that whatever Casimir work is done in the compressive part of the cycle is returned in the elastic reaction, giving a Casimir force with no external effect.

As described in the introduction, in a stack of alternating tunably conductive and piezo layers, the Casimir force might be equated to the material tension, which represents a static piezo response, relevant when the piezo layer is acoustically isolated from the rest of the stack and incommensurate in scale compared to the acoustic wavelength. The Casimir tension is on during the conductive or compressive part of the forcing cycle and off during the nonconductive elastic response, and thus maps out the area W as defined in Eq. (2) in the T-S phase space. As that calculation simply took the stress T to be proportional to the strain S and ignored the additional electrical displacement contribution D in (32) representing the converse piezo effect, it needs to be increased by a multiplicative factor $1 + k_{\rm p}$, equating the amplitudes of the total mechanical work and dielectric energies from (31). The piezo coupling constant $k_{\rm p}$ is defined in Section 6.31 of Mason 1966 [32]. It is typically small, $k_{\rm p} \sim 0.1$ in Mason's example.

In general the Casimir force $F(z,t)$ in a permittivity wave in a crystal acts to introduce coupled stress T_{ij}, strain S_{ij}, electric field E_i, and electric displacements D_i, which depend upon the orientation of the natural crystal axes with respect to the acoustic wave z axis of the system. The attractive Casimir force per unit area is a traction force that acts internally in the crystal in the z direction and only as a function of z in our plane-parallel approximation, and thus must satisfy the force balance equation [34, Section 2.B]

$$\rho\frac{\partial^2 u_i}{\partial t^2} - \frac{\partial T_{ij}}{\partial x_j} = \frac{\partial F(z,t)}{\partial z}\delta_{(iz)}, \tag{34}$$

with ρ the density of the medium, and u_i the particle displacement 3 vector. In addition the spatially varying component to D_z must vanish due to Maxwell's equation in an acoustic wave for charge conservation, written for a nonconducting medium as $\nabla \cdot \{D_i\} = \partial D_i/\partial x_i = 0$, denoting the vector of elements as $\{D_i\}$, which reduces to its z component $\partial D_z/\partial z = 0$ when $\partial/\partial x = \partial/\partial y = 0$ as we suppose everywhere in the interior of the crystal. Also Maxwell's vanishing curl of the electric field in an acoustic field $\nabla \times \{E_i\} = 0$, requires that the spatially varying transverse electric field in (E_x, E_y) also be zero.

Particle displacements define the strain tensor

$$S_{ij} = \frac{1}{2}\left(\frac{\partial u_i}{\partial x_j} + \frac{\partial u_j}{\partial x_i}\right), \tag{35}$$

which, for vanishing x and y derivatives everywhere in the interior of the crystal, gives the Casimir-force driving equations for the three nonvanishing strain elements S_{zz}, S_{xz}, and S_{yz}, by taking the z derivative of (34)

$$\rho\frac{\partial^2 S_{zz}}{\partial t^2} - \frac{\partial^2 T_{zz}}{\partial z^2} = \frac{\partial^2 F(z,t)}{\partial z^2}, \tag{36}$$

$$2\rho\frac{\partial^2 S_{iz}}{\partial t^2} = \frac{\partial^2 T_{iz}}{\partial z^2}, \tag{37}$$

for $i = x, y$.

Using Eq. (33) to eliminate the tension terms in the force equations (36) and (37) defines the strain for a given Casimir force F and electric displacement D_i, for S_{zz}

$$\rho\frac{\partial^2 S_{zz}}{\partial t^2} - c^D_{zziz}\frac{\partial^2 S_{iz}}{\partial z^2} = \frac{\partial^2}{\partial z^2}\left(F(z,t) - h_{izz}D_i\right), \tag{38}$$

and for S_{xz} and S_{yz}

$$2\rho\frac{\partial^2 S_{iz}}{\partial t^2} - c^D_{izjz}\frac{\partial^2 S_{jz}}{\partial z^2} = -h_{jiz}\frac{\partial^2 D_j}{\partial z^2}. \tag{39}$$

The set of coupled linear differential equations are simplified by Fourier and eigenvalue analyses. Only strain waves and electric displacements at the frequency 2ν for the Casimir forcing are relevant, but because of the Casimir bulk mode in the driving force from (25), a general spectrum of wavenumbers k_z are possible. We analytically continue by supposing the complex temporal variation in every term $\exp(i4\pi\nu t)$ and Fourier transform with spatial z functions going over into wavenumber k_z functions denoted by overbars. Then diagonalizing the matrix that multiplies the longitudinal/shear strain vector $(\bar{S}_{xz}(k_z), \bar{S}_{yz}(k_z), \bar{S}_{zz}(k_z))$ from the left sides of Eqs. (38) and (39) gives eigenvalue equations for at most three independent strain eigenvectors

$$\bar{S}(k_z) = \frac{k_z^2}{k_{z0}^2 - k_z^2}\left(\varphi\bar{F}(k_z) + h\bar{D}(k_z)\right); \tag{40}$$

where the stain eigenstate is denoted $\bar{S}(k_z)$. The Casimir forcing function is denoted $\bar{F}(k_z)$ with φ a factor that projects the purely longitudinal z force into the strain eigenvector, and the projection of the shear electric displacement (D_x, D_y) written $\bar{D}(k_z)$ with its projection into the eigenvector contained in the single scalar coefficient h for the effective piezo force. The resonant wavenumber is defined $k_{z0} = 4\pi\nu/c_\mathrm{s}$ for a sound speed c_s that contains the density ρ and the crystal stiffness from $c^D_{ijk\ell}$ for the eigenvector. The common temporal variation $\exp(i4\pi\nu t)$ has been factored out of each of the terms, but possible temporal phase delays for the strain and electric displacement compared to the Casimir forcing may be contained as complex factors $\exp(i\delta_S)$ or $\exp(i\delta_D)$ in the functions $\bar{S}(k_z)$ and $\bar{D}(k_z)$.

A transfer of energy between the mechanical and dielectric terms occurs if the integral of $T_{ij}dS_{ij}$ (or equally $-E_{ij}dD_{ij}$) over a cycle is nonzero. As can be seen by

examining T-S phase diagrams, if the strain lags behind the stress, the integral TdS is positive and mechanical work is converted to dielectric energy. In some processes it is possible that the strain may lead the stress, corresponding to the transfer from an external electrical load into the quantum zp. The possible electric displacement and electric fields are defined by the boundary conditions, and by their coupling to the stress and strain from (32) and (33), but with phase delays that depend upon the external circuit load.

We examine the piezo energy transfer arising with the Casimir wave and bulk modes for a permittivity wave in a uniform medium from (25) of Section 3. A strain wave eigenstate may be driven as described in Eq. (40) by the Casimir wave (standing or traveling) from (25) at wavenumber $k_z = |4\pi/\lambda|$ if it is near resonance with the vanishing denominator at $k_z = k_{z0} = 4\pi\nu/c_{\rm s}$. Resonance thus requires that $\lambda = \nu/c_{\rm s}$, or that the sound speed for the acoustic wave is the same as that for the strain eigenstate, which has twice the frequency (and wavenumber). However high frequency acoustic waves with wavelength much smaller than the scale of the crystal do not normally couple capacitively anyway, as the spatially varying displacement field D_i must be perpendicular to the wave direction and the electric field E_i parallel, and being always mutually perpendicular can do no work in the energy Eq. (31). We can imagine certain exotic arrangements perhaps like what is described in the literature [35] that may allow piezo coupling to the main Casimir wave mode. However with such arrangements it may be difficult to avoid dissipating the acoustic wave too that drives the Casimir effect.

The Casimir bulk mode for standing waves from (25) couples more straightforwardly. That mode is described as a spatial boxcar between uniform z-facing electrodes as in the drawing Figure 2. Charge buildup on the electrode surfaces defines a boxcar function too for the electric displacement $D_z(t)$ giving sinc functions in the k_z Fourier domain for $\bar{F}(k_z)$ and $\bar{D}(k_z)$ in (40). Thus the strain $\bar{S}(k_z)$ is proportional the multiplier $k_z^2/(k_{z0}^2 - k_z^2)$ times a sinc function in wavenumber space. Both functions are illustrated in Figure 12.

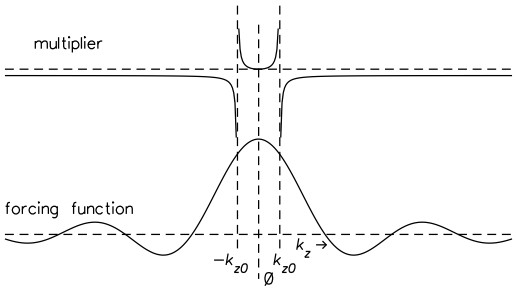

Figure 12. Wavenumber-space multiplier and forcing function for a strain response comparable in scale to the dimension of the crystal.

If the resulting strain spatial function $S(z)$ is small in magnitude compared to the electric displacement for the projected eigenstate $|S(z)| \ll |D(z)|$ over z, then the stress $T(z)$ and electric field $E(z)$ are determined solely by the electric displacement using

the constitutive relations (32) and (33), and significant phase differences between the quantities are precluded, so no energy transfer possible. The total mechanical work done through the volume in a wave cycle is determined by the spatial-temporal integral of $T(z,t)\partial S(z,t)$, which feels its determining contribution from the spatial-temporal integral of $S(z,t)$ times the boxcar forcing. By the Fourier power theorem, the spatial integral can be equated to a wavenumber integral of the multiplier for $\bar{S}(k_z,t)$ from (40) times a sinc function squared. As long as strain variations are on the scale of the crystal, the integral over wavenumber of the product of the two functions is large and comparable to what would be obtained if the strain response were a pure boxcar. A significant strain response to longitudinal boxcar forcing on the scale of the crystal thus requires a small wavenumber $k_{z0} \sim 0$ corresponding to a wavelength for the eigenstate comparable to the size of the crystal. Characteristically phonon optical modes do exhibit zero wavenumber crossings corresponding to the Brillouin zone center at around 10 THz frequency in crystals [31, Chapter 3].

Perpendicular uniform surface electrodes say in x might be effective too, as electric displacement $D_y(z)$ and electric fields $E_y(z)$ constant in y may strongly couple to the induced strain field $S(z)$. As the Casimir forcing is everywhere one directional, power generation must be relatively tolerant against incoherence in the standing waves due to partial or incomplete acoustic wave reflection, crystal imperfections, or acoustic attenuation effects.

The voltage difference between electrodes is defined by the electric field, the order of which is determined by the piezo relation $E \sim gT \sim -gF$ for g the piezoelectric voltage constant; characteristically $g \simeq$7E$-$5 Volt cm/dyn for crystals. For a strength of Casimir bulk mode from Figure 10 of around 5E8 dyn/cm^3, we estimate an electric field of E=35000 V/cm, which gives a current of 28.6 Amperes per cm^2 of electrode surface area for a nominal total power of 1 MW/cm^3, which is the product of the two.

Though it has not been our main interest, stacks of alternating layers, the basis for our thought experiment, might give another practical design for a crystal power generator. A stack of alternating p- and n-doped piezo semiconductor layers are conductive throughout except in the depletion zones between the layers, which may be tuned conductively via electric or light fields. The design satisfies the need for fast and easy tuning as semiconductors operating differentially at p- to n- doped junctions exhibit a low excitation potential, and the Casimir force across the thin nonconductive depletion zone between conductive layers exhibits a strong piezo effect in many semiconductor materials. Fine tuning of the material parameters, doping concentrations, layer thicknesses, and frequency are needed to fix the thickness of the depletion zone. The light-travel distance c/ν= 30 μm for ν=10 THz is smaller than the size of multilayer stacks of interest, but larger than a useful layer thickness, but the stack need not be modulated in-phase. With slow in-phase cycling, an AC voltage across the total stack area and thickness is produced, whereas fast out-of-phase cycling feels differing contributions across the stack at any one time giving a more nearly DC voltage.

7. Power Estimates

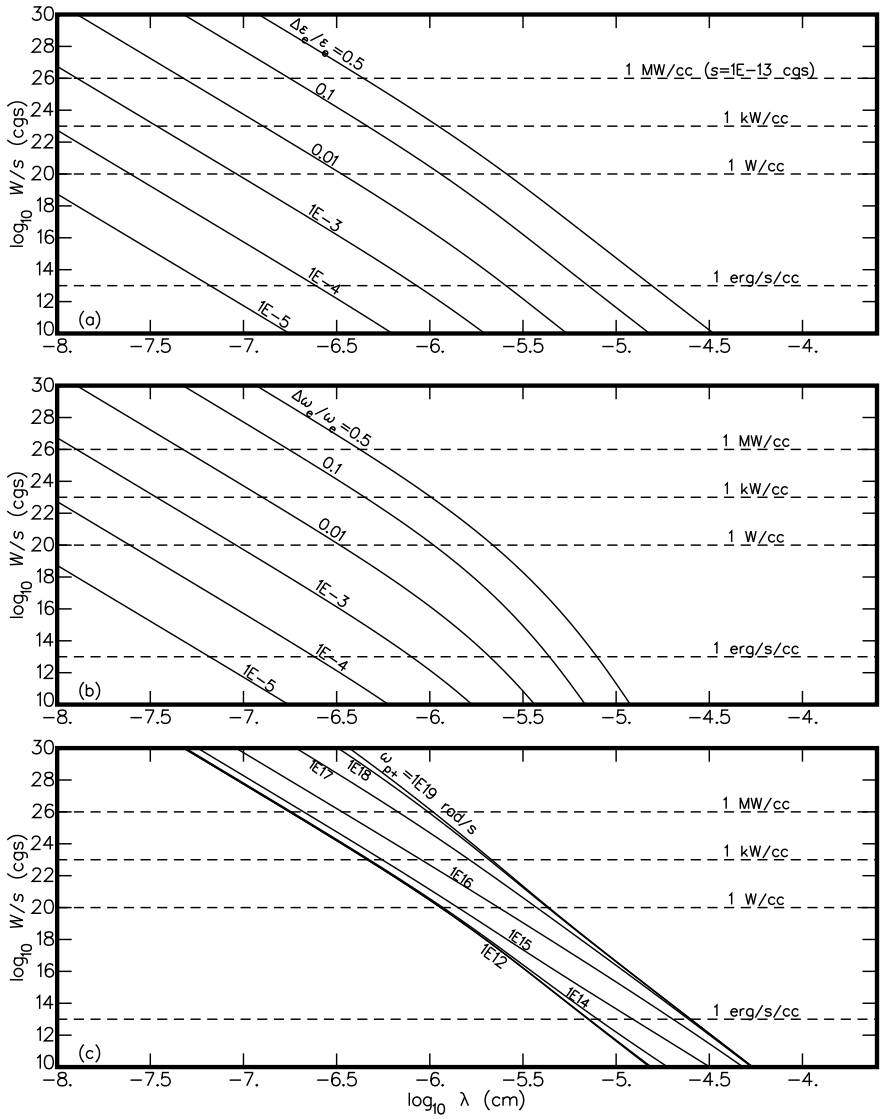

Figure 13. Available power per unit of crystal volume W as function of layer thickness $\lambda = \ell_- + \ell_+$ with $\ell_+ = \ell_-$ in a stack with alternating static permittivity (a), electronic vibration frequency (b), and plasma frequency (c) for modulation at frequencies corresponding to the sound speed $c_s = \nu\lambda$=5E5 cm/s. Horizontal power levels (*dashed*) are for material compliance s=1E−13 cm^2/dyn.

A stack of alternating layers cycled at a rate ν produces a Casimir forcing that cycles at twice that rate 2ν as discussed at the end of Section 4. Thus our estimate for the maximum power that might be extracted represented by the formula (2) needs ν replaced by 2ν. Noting too the participation of the full volume in the process and supposing equal even-odd layer thicknesses $\ell_+ = \ell_-$, we obtain

$$W = s\nu F^2. \tag{41}$$

The formula ignores the small force difference $\Delta F \ll F$ between the two half cycles.

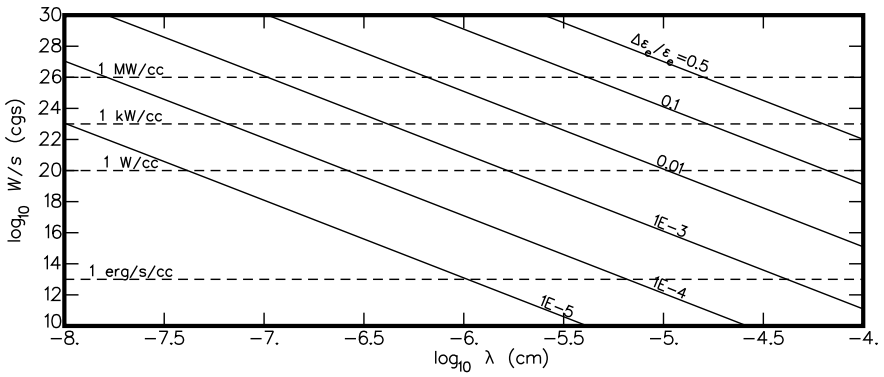

Figure 14. Available power per unit of crystal volume W as function of wavelength λ in a static-permittivity wave of indicated contrast for modulation at frequencies ν defined by the sound speed $c_s = \nu\lambda$=5E5 cm/s. Horizontal power levels (*dashed*) are for a material compliance s=1E−13 cm^2/dyn.

Figure 13 gives estimates of the available power from (41) for modulating the static permittivity ε_e (*panel* (a)), the electronic frequency ω_e (b), and the plasma frequency (c), using the numerical computations from Section 4 supposing the acoustic relation between frequency and wavelength $\nu = c_s/\lambda$, and using a sound speed c_s=5E5 cm/s, characteristic of dense materials at least at frequencies below 2 THz, or λ=2.5E−7 cm=2.5 nm. The varying dispersion and possible phonon modes at small wavelengths may change greatly the appearance of the figure, but power levels should be representative. The available power goes like the Casimir force squared, and so drops quite rapidly with λ, and also depends quite critically on the relative permittivity fluctuation going as the 4th power.

Estimates for the plasma frequency modulation in (c) are similar in their maximum values, but form a relatively tight group for the range of possible plasma frequencies. For an idealized perfect conductor with plasma frequency above ω_p=1E18 rad/s, the curves show little change, and represent an available power of about 1 MW/cm^3 with ℓ_0=5 nm (λ=10 nm=1E−6 cm), for the conservative piezo compliance s=1E−13 cm^2/dyn, consistent with the estimate given in the introduction. However power levels drop off rapidly when the plasma frequency contrast is less than 1E18 rad/s as with normally conductive materials, which exhibit plasma frequencies only as high as 1.6E16 rad/s.

Figure 14 shows power per unit volume W from (41) for the main Casimir modes, the bulk mode $\tilde{F}_0$ or main wave mode $\tilde{F}_{2c}$ as they are of equal amplitude, as a function of the acoustic wave wavelength for static-permittivity fluctuations of differing relative strength. The figure illustrates the high power levels that are possible even with a modest relative permittivity wave amplitude of $\Delta\varepsilon/\varepsilon$=1E−3 and shows the much greater range into longer wavelengths for the permittivity waves compared to multilayer stacks. Such amplitudes are easily below normal crystal damage thresholds [20].

8. Mode Growth and Attenuation

Casimir modes should arise in any material, not just a piezo crystal, and may feed back producing either growth or attenuation in the principle acoustic wave. An acoustic wave exhibits an associated permittivity variation due to the acousto-optic effect, which is determined phenomenologically by the Pockels second-order nonlinear response due to the piezo-induced electric field caused by an acoustic wave of pressure amplitude $\tilde{P}$

$$\frac{\Delta\varepsilon}{\varepsilon} = \varepsilon p s \tilde{P}, \tag{42}$$

with s the material compliance relevant for the propagation direction and shear. The photoelastic coefficient p is a dimensionless parameter for the material in the wave direction for an unsheared or sheared stress for longitudinal or transverse waves, respectively; characteristically $p \sim 0.1$ and usually positive.

The Casimir mode $\tilde{F}_{1c}$ must always couple linearly to the principle acoustic wave as it is of same frequency and wavenumber. For materials of positive photoelastic coefficient p, the acousto-optic effect from (42) exhibits a pressure variation correlated with the induced permittivity wave $\varepsilon(z)$, giving a Casimir wave mode $\tilde{F}_{1c}$ with the same sign as the pressure in the acoustic wave and so amplifying. But in materials of negative photoelastic coefficient $p < 0$, such as GaAs or Ruby, the Casimir wave mode $\tilde{F}_{1c}$ is dissipative. In each acoustic wave cycle for standing or traveling waves at a given spatial location, the Casimir mode $\tilde{F}_{1c}$ is generated from quantum zp energy and forces the principle acoustic wave. All of the energy in the Casimir mode $\tilde{F}_{1c}$ feeding into the pressure wave amplitude $\tilde{P}$ gives the maximum growth rate

$$\Gamma_{1c} = \frac{\partial \ln \tilde{P}}{\partial t} = 2\pi\nu \frac{\tilde{F}_{1c}}{\tilde{P}}. \tag{43}$$

Taking $\tilde{F}_{1c}$ from (29) with $\tilde{P}$ from (42), and using the static-permittivity fluctuation for the permittivity variation $\varepsilon \to \varepsilon_e$ with the result from Figures 8-10 that $\tilde{F}_{1c}/\tilde{F}_0 = \Delta\varepsilon_e/\varepsilon_e$, we obtain

$$\Gamma_{1c} = \frac{\pi^2 \hbar \omega_e \omega_c}{32c} \frac{p s \varepsilon_e^{3/2} \nu^3}{c_s^2} \left(\frac{\Delta\varepsilon_e}{\varepsilon_e}\right)^2 = \left[\frac{\nu}{0.216 \text{ GHz}}\right]^3 \left(\frac{\Delta\varepsilon_e}{\varepsilon_e}\right)^2, \tag{44}$$

now using the acoustic wave frequency ν rather than its wavelength λ in the formula, with sound speed $c_s = \lambda\nu$, and using characteristic parameters for the rightmost equality p=0.1, s=1E−13 cm^2/dyn, c_s=5E5 cm/s, ω_e=2E16 rad/s, ω_c=7.76E20 rad/s, the Compton frequency, and ε_e=6. The growth rate represents an amplitude e-folding in a distance c_s/Γ for the often-used attenuation factor $\alpha = -(20 \log e)\Gamma/c_s$ dB, giving

$$\alpha_{1c} = -\left[\frac{\nu}{35.3 \text{ GHz}}\right]^3 \left(\frac{\Delta\varepsilon_e}{\varepsilon_e}\right)^2 \text{dB/cm}, \tag{45}$$

in units of decibels per cm. For a wave of frequency $\nu = 1$ THz and high amplitude $\Delta\varepsilon_e \simeq \varepsilon_e$, we obtain a maximum growth rate of 28 dB/cm. The growth rate drops off rapidly with decreasing acoustic wave amplitude going as $(\Delta\varepsilon_e/\varepsilon_e)^2$.

Unless it is an phonon eigenstate, the primary Casimir mode $\tilde{F}_{2c}$ will be strongly dissipated by interference from out-of-phase driving by $\tilde{F}_{2c}$ modes in adjacent wavelengths of the principle acoustic wave, leading to a rapid exponential attenuation rate. Though of frequency 2ν, the mode $\tilde{F}_{2c}$ is coherent with the principle acoustic wave and might exchange energy effectively with it if there is a sufficient nonlinear interaction between the two. Coherent acoustic modes may exhibit nonlinear interactions similar to coherent electromagnetic states, which exchange energy easily between overtones, and generally satisfy a principle of energy equipartition [36]. If there is a strong coupling, the attenuation rate for the principle acoustic wave may be as much as half the $\tilde{F}_{2c}$ mode amplitude per acoustic wave cycle to give an attenuation rate or negative growth rate in the principle acoustic wave a factor $(\Delta\varepsilon_e/\varepsilon_e)$ larger than the growth rate for the smaller $\tilde{F}_{1c}$ mode from (43) – (45). Such attenuation would go like ν^3 and be nonlinear as it depends upon the mode amplitude.

If the Casimir mode $\tilde{F}_{2c}$ is a longitudinal phonon eigenstate, it may similarly affect growth in the principle acoustic wave of comparable magnitude. Thus it may be desirable to match frequencies and crystal orientations in materials where both of the main Casimir modes with frequency 2ν are phonon eigenstates: the bulk mode with wavenumber $k_z \sim 0$ and wave mode of wavenumber twice that of the acoustic wave. Further discussion on the growth or attenuation of the principle acoustic wave that might be caused by Casimir modes is material dependent and discussion of possible nonlinear interactions seems beyond the scope of this paper.

Noncrystalline substances do exhibit a limiting high-frequency attenuation that increases faster than ν^2 and appears to be close to a ν^3 form [37, Figure 10]. Though such measured THz attenuation factors are much larger than ours, these are for noncrystalline substances, which are known to exhibit a much stronger acoustic attenuation than what is seen in pure crystals [38, 39, 40]. Attenuation effects exhibit a strong temperature dependence below 100 GHz, but become temperature independent above that frequency, as we expect for Casimir modes. Measured attenuation effects in noncrystalline materials are found to have a nonlinear amplitude dependence at least at 10 GHz frequency [39].

9. Conclusion

We have studied the Casimir effect in multilayer stacks and in graded-permittivity media both analytically and with numerical models. In a stack of alternating high- and low-permittivity layers, an attractive Casimir force is produced throughout the volume, which follows closely solutions for a three-layer sandwich, with thin- and thick- central-layer ℓ_0 limiting power-law forms that go like $1/\ell_0^3$ and $1/\ell_0^4$, respectively. The Casimir force switches power laws at fairly small scales depending upon the permittivity contrast, as at thickness ~ 7 nm for usual parameters. The compressive force is only slightly smaller across the high-permittivity layers than across the low-permittivity layers. By modulating the permittivity in the layers, it is possible to cycle the Casimir force on and off through the volume and harvest energy in each cycle by the piezo effect. The concept

might be implemented in a stack of alternating p- and n- doped piezo semiconductor layers, which are conductive and might rapidly tune the conducting state of depletion zones between the layers by an electric field or light.

Similarly a short wavelength permittivity wave in a uniform material produces large Casimir half-wavelength and bulk expansive modes. The Casimir effect in a 1 nm acoustic wave is about 1000 times stronger than that found in a stack of alternating layers of the same permittivity contrast and scale of variation, and extends to much larger scales decreasing only as $1/\lambda^2$. The Casimir effect in a wave does not feel a natural frequency cutoff as arises across a uniform layer due to retardation extinction, but feels contributions out to the frequency cutoff for the zp interactions, which we take to be the Compton frequency. Smaller amplitude Casimir modes arise too as higher wavenumber overtones of the principle wave with amplitudes proportional to increasing powers of the relative permittivity contrast. Unlike for a multilayer, the Casimir effect in a permittivity wave exhibits no temperature dependence at least within the scope of our numerical models.

Casimir modes induced by THz acoustic waves in a piezo crystal may couple effectively to an external electrical circuit, in effect taking energy out of, or returning it to the quantum zp, as we have shown through the piezo thermodynamic formalism. A significant energy transfer is possible for standing acoustic waves of frequency ν through the Casimir bulk mode, but only if matched to a low wavenumber eigenstate at frequency 2ν, like a phonon optical mode. Acoustic waves might be introduced and coherently maintained in different ways, like by shining monochromatic microwave light on one or opposite piezo crystal surfaces through transparent electrodes [41]. The standing wave coherence that is possible for nm waves might be greatly limited by surface or crystal imperfections, or other sources of acoustic attenuation. However since the Casimir bulk mode is expansive, the voltage effect is single signed and so should add constructively through the volume with partially coherent standing waves for a partial ac or dc voltage difference across the crystal.

We estimate that significant power may be derived of maximum order a MW/cm^3 for 1 nm=1E−7 cm wave even with a modest relative permittivity contrast of 1E−3. A significant effect persists even out to 100 nm acoustic wavelengths due to the slow falloff of the Casimir force with wavelength. Casimir modes may be important in the attenuation or driving of hypersonic (10 GHz - 10 THz) acoustic waves through nonlinear or direct linear feedback, as we have discussed.

Author's Note

It is the author's expressed intent that the guidance, concepts, and designs described remain unpatentable but in the public domain. It is his belief that energy derived from the quantum zp is God given for the free and beneficial use by all on His good earth.

Appendix A. Limiting Solutions for Multilayer Stacks

Power laws arise for the Casimir force in the thin- and thick-layer limits for certain forms of permittivity variations. In this appendix, we parallel the Lifshitz derivation [12, 21] for the Casimir force integral from (6) for permittivity variations defined by contrasts in each of the parameters contained in (27).

A rearrangement of the Casimir force integral in (6) facilitates evaluation of the force in the middle layer. Using the new variable $\chi = 2\kappa_0\ell_0 = (\varepsilon_0(\xi)\xi^2 + \varpi^2)^{1/2}\ell_0/c$ to eliminate κ_0 under the integral, and substituting for the integration variable ϖ using $d\chi^2 = (4\ell_0^2/c^2)d\varpi^2$, gives

$$F = \frac{\hbar}{16\pi^2\ell_0^3}\int_0^\infty\int_0^\infty \chi^2\left(Д_s + Д_p\right)d\chi d\xi. \tag{A.1}$$

denoting layers by subscript number with ℓ_0, ε_0, and κ_0 for the middle layer. The force integral in (A.1) is dominated by the single value $\chi \simeq 1$ due to the tradeoff between the χ^2 weighting factor under the integral, which increases with χ, and the decreasing exponential $\exp(-2\kappa_0\ell_0) = \exp(-\chi)$, which determines the reflection terms $Д_{\binom{s}{p}}$ in (4), through the products of Fresnel reflection coefficients from Eq. (11).

As Lifshitz points out [12], when the middle layer is sufficiently thin $\ell_0 \ll c/\omega_\mathrm{e}$, the dominant wavenumber $\kappa_0 \sim 1/\ell_0$ is higher than the wavenumber for electronic vibrations $\kappa_0 \gg \omega_\mathrm{e}/c$. The permittivity $\varepsilon_j(\xi)$ between layers changes little at frequencies $\xi \gg \omega_\mathrm{e}$ as is evident in Eq. (27), so the wavenumber between layers κ_j changes little too. The jump coefficients $r_{s\pm}$ from (8) contribute little to the integral, and s polarization effects and $Д_s$ can be ignored. Also dependencies upon κ in the p polarization jump coefficients $r_{p\pm}$ from (9) or in $Д_p$ divide out. Taking contributions from only the nearest jump in the Fresnel reflection terms, and dropping the product of reflection coefficients from the denominator of $Д_p$ in (4), as it introduces a fourth-order effect in the relative permittivity change compared to the main second-order effect, we obtain the Lifshitz thin-layer Casimir force formula written for permittivities symmetric about a middle $j = 0$ (Eq. (4.18) [21])

$$F_\langle = \frac{\hbar}{8\pi^2\ell_0^3}\int_0^\infty \left(\frac{\Delta\varepsilon(\xi)}{\varepsilon(\xi)}\right)^2 d\xi. \tag{A.2}$$

using a compact notation to denote the permittivity contrast $\Delta\varepsilon = (\varepsilon_0 - \varepsilon_{\pm1})/2 = (\varepsilon_- - \varepsilon_+)/2$, and the average $\varepsilon = (\varepsilon_0 + \varepsilon_{\pm1})/2 = (\varepsilon_- + \varepsilon_+)/2$ for layers numbered 0, ±1, even $-$, or odd $+$. As the permittivity $\varepsilon(\xi)$ does not depend upon χ, the χ integral factors out in the derivation as a Gamma function $\int_0^\infty \chi^2 e^{-\chi}d\chi = 2$.

Supposing that the permittivity contrast arises due to static-permittivity fluctuations $\Delta\varepsilon = (\partial\varepsilon/\partial\varepsilon_\mathrm{e})\Delta\varepsilon_\mathrm{e}$ for permittivities defined in (27), we obtain an analytic integral in (A.2) with the solution

$$F_\langle = \frac{\hbar\omega_\mathrm{e}\sqrt{\varepsilon_\mathrm{e}}}{32\pi\ell_0^3}\left(\frac{\Delta\varepsilon_\mathrm{e}}{\varepsilon_\mathrm{e}}\right)^2, \tag{A.3}$$

assuming a nonconductor $\omega_\mathrm{p} = 0$ for simplicity. The thin-layer limiting force with a fluctuating electronic vibration frequency $\Delta\varepsilon = (\partial\varepsilon/\partial\omega_\mathrm{e})\Delta\omega_\mathrm{e}$ similarly gives

$$F_\langle = \frac{\hbar\omega_\mathrm{e}}{8\pi\ell_0^3}\frac{(\varepsilon_\mathrm{e}-1)^2}{(\varepsilon_\mathrm{e}^{1/2}+1)^3}\left(\frac{\Delta\omega_\mathrm{e}}{\omega_\mathrm{e}}\right)^2. \tag{A.4}$$

Corresponding limiting behavior with varying plasma frequency or Drude parameter is less obvious, as suggested in the numerical solutions described in Section 4.

When the middle layer is sufficiently thick, the main contribution to the Casimir force in (A.1) comes from low frequencies, and wavenumber changes from layer to layer cannot be ignored. If static-permittivity variations exist, then it seems a good approximation to suppose that the permittivity is constant in frequency and well approximated by its static value $\varepsilon(\xi = 0)$. A critical integral substitution allows all of the variables of the problem to factor out and renders the integral essentially constant over parameter ranges of interest. Such a substitution is suggested by the behavior of the jump coefficients r_{s-} in the low-frequency limit, which are equal to the wavenumber contrast between layers $r_{s-} = \Delta\kappa/\kappa$. Differentiating κ with respect to ε in the wavenumber definition in (5) allows us to translate the wavenumber contrast into a static-permittivity contrast as

$$\frac{\Delta\kappa}{\kappa} = \left(\frac{\xi\sqrt{\varepsilon(0)}}{2c\kappa}\right)^2\frac{\Delta\varepsilon(0)}{\varepsilon(0)} \simeq \left(\frac{\nu}{\chi}\right)^2\frac{\Delta\varepsilon(0)}{\varepsilon(0)}, \tag{A.5}$$

where $\chi = 2\kappa_0\ell_0 \simeq 2\kappa\ell_0$ for small fluctuations $\Delta\kappa/\kappa$, and defining a new variable $\upsilon = \xi\ell_0\sqrt{\varepsilon(0)}/c$. By substituting the new variable υ for ξ, the wavenumber contrast becomes consolidated into a permittivity contrast with dimensionless coefficients defined by the variables of integration. Such a substitution indeed factors out all spatial scale dependencies and simplifies the integral in (A.1), giving

$$F_\rangle \simeq \frac{\mu\hbar c}{\sqrt{\varepsilon(0)}\ell_0^4}\left(\frac{\Delta\varepsilon(0)}{\varepsilon(0)}\right)^2. \tag{A.6}$$

with the coefficient μ approximately constant over a wide range of static permittivity contrasts. Lifshitz has shown this simplification to an equivalent expression for noninfinitesimal permittivity contrasts, which leads to a nonanalytic exponential-type integral he denotes $\phi_\mathrm{dd}(\varepsilon_1(0)/\varepsilon_0(0))$, which relates to our coefficient $\mu = (\pi^2/240)\phi_\mathrm{dd}(1+2\Delta\varepsilon(0)/\varepsilon(0))$, writing the argument of ϕ_dd for small static-permittivity fluctuations $\Delta\varepsilon(0) \ll \varepsilon(0)$. He evaluates the integral numerically and obtains $\phi_\mathrm{dd} = 0.35$ for $\varepsilon_1(0)/\varepsilon_0(0) \gtrsim 0.3$ (Eq. (4.22) [21]), which gives $\mu = 0.0144$ for relative static-permittivity fluctuations $\Delta\varepsilon(0)/\varepsilon(0) \gtrsim -0.35$. From the Lifshitz more general formulation, when the sandwiching layers are nonconductors with large permittivity contrast $|\Delta\varepsilon_\mathrm{e}| \gg \varepsilon_\mathrm{e}$ or pure conductors, the Casimir force is approximated as $F_\rangle$ in (1) discussed in the introduction.

Only as long as the main permittivity fluctuations have a low-frequency component, as in fluctuations of the static permittivity ε_e, the plasma frequency ω_e, or the Drude collision frequency Γ_p does the limiting thick-layer solution form (A.6) apply. It does not

apply with permittivity fluctuations produced by fluctuations of the electronic vibration frequency ω_e as illustrated in the numerical examples from Section 4.

The cross-over thickness between the two power laws $\ell_{\langle\rangle}$ is defined as $F_\langle(\ell_{\langle\rangle}) = F_\rangle(\ell_{\langle\rangle})$. Using (A.3) and (A.6) for static-permittivity fluctuations, we obtain

$$\ell_{\langle\rangle} = 1.448\frac{c}{\omega_\mathrm{e}\varepsilon_\mathrm{e}}, \tag{A.7}$$

supposing that a permittivity contrast arises due to static-permittivity fluctuations with $\Delta\varepsilon(0) = \Delta\varepsilon_\mathrm{e}$ and $\varepsilon(0) = \varepsilon_\mathrm{e}$. For the case in Figure 5 with ω_e=2E16 rad/s and ε_e=6, we obtain $\ell_{\langle\rangle}$=3.62E−7 cm or $\lambda_{\langle\rangle}$=7.24E−7 cm=7.24 nm=E−6.14 cm, in good agreement with the intersection of lines seen in the figure. The cross-over distance decreases with increasing static permittivity, suggesting a smaller cross-over distance in more conductive media.

Appendix B. Computational Considerations with a Graded Medium

Calculations of the Casimir effect in a medium with a small amplitude graded 1D permittivity variation are based upon the force integral Eq. (6) with (4), with Fresnel reflection coefficients defined by the integral (16) with (14) and (15). For numerical calculations the spatial integral in (16) is best defined in the specific way

$$R_{\binom{s}{p}_-}(z) = \Upsilon_{\binom{s}{p}_-}(z) + e^{-2\int_{z_a}^{z}\kappa(z')dz'}C_{\binom{s}{p}_-}, \tag{B.1}$$

where

$$\Upsilon_{\binom{s}{p}_-}(z) = \int_{z_b}^{z} e^{2\int_{z_a}^{z'}(\kappa(z'')-\kappa(z))dz''} r_{\binom{s}{p}_-}(z')\left(1 - R'_{\binom{s}{p}_-}(z')^2\right)dz', \tag{B.2}$$

now including lower bounds on the integrals z_a for the integrating factor and z_b for the main integral. The lower bounds are arbitrary, and $C_{\binom{s}{p}_-}$ is a constant of integration. We have taken the external exponential factor under the integral, which is a form more suitable for numerical calculations, as the wavenumber difference helps avoid very large exponential factors at the limits of normal computer precision that arise in integrals of the wavenumber $\kappa(z)$. Integrals over a full long wave λ=1 μm are of order 1E6 at the highest frequencies ϖ=6E20 rad/s, which would lead to cancelling exponential factors of order exp(1E6).

Periodic solutions of wavelength λ require the condition $R_{\binom{s}{p}_-}(z_c) = R_{\binom{s}{p}_-}(z_c+n\lambda)$ for any origin z_c and integer n. The condition uniquely determines the constant of integration $C_{\binom{s}{p}_-}$, since the solutions must be periodic, as we have described in Section 3. Substituting with (B.1) then gives, with careful handling of the limits of integration in the sums and differences of integrals that arise, the expression

$$e^{-2\int_{z_a}^{z}\kappa(z')dz'}C_{\binom{s}{p}_-} = e^{-2\int_{z_c}^{z}\kappa(z')dz'}\left(\frac{\Upsilon_{\binom{s}{p}_-}(z_c+\lambda) - \Upsilon_{\binom{s}{p}_-}(z_c)}{1 - e^{-2\int_{z_c}^{z_c+\lambda}\kappa(z')dz'}}\right). \tag{B.3}$$

Using this form to represent the constant of integration avoids other possible occurrences of large exponential factors. The term is the offset in (B.1), which may be directly added

to the integrals $\Upsilon_{\binom{s}{p}_-}(z)$ to give periodic solutions for the Fresnel reflection coefficients $R_{\binom{s}{p}_-}(z)$.

[1] Milonni P W 1994 *The Quantum Vacuum, An Introduction to Quantum Electrodynamics* (San Diego, CA: Academic Press, Inc.)

[2] Schwinger J 1951 On Gauge Invariance and Vacuum Polarization *Phys. Rev.* **82** 664–679

[3] Parker L 1969 Quantized Fields and Particle Creation in Expanding Universes. I *Phys. Rev.* **183** 1057–1068

[4] Cole D C and Puthoff H E 1993 Extracting energy and heat from the vacuum *Phys. Rev. E* **48** 1562–1565

[5] Forward R L 1984 Extracting electrical energy from the vacuum by cohesion of charged foliated conductors *Phys. Rev. B* **30** 1700–1702

[6] Pinto F 1999 Engine cycle of an optically controlled vacuum energy transducer *Phys. Rev. B* **60** 14740–14755

[7] Haisch B and Moddel G 27 May, 2008 Quantum vacuum energy extraction *US Patent* 7,379,286

[8] Casimir H B and Polder D 1948 The Influence of Retardation on the London-van der Waals Forces *Phys. Rev.* **73** 360–372

[9] Casimir H B 1948 On the Attraction between Two Perfectly Conducting Plates *Proc. K. Ned. Akad. Wet.* **51** 793–795

[10] Caride A O, Klimchitskaya G L, Mostepanenko V M and Zanette S I 2005 Dependences of the van der Waals atom-wall interaction on atomic and material properties *Phys. Rev. A* **71** 042901 (*Preprint* `arXiv:quant-ph/0503038`)

[11] Klimchitskaya G L, Mohideen U and Mostepanenko V M 2009 The Casimir force between real materials: Experiment and theory *Rev. Mod. Phys.* **81** 1827–1885 (*Preprint* `0902.4022`)

[12] Lifshitz E M 1956 The Theory of Molecular Attractive Forces Between Solids *JETP* **2** 73–83

[13] Cooke M 2007 Filling the THz gap with new applications *Semiconductor Today* **2** 39–43

[14] Inui N 2003 The Casimir Energy of a Medium Containing a Permittivity Gradient *J. Phys. Soc. Jpn.* **72** 280–286

[15] Podgornik R and Parsegian V A 2004 Van der Waals interactions in a dielectric with continuously varying dielectric function *J. Chem. Phys.* **121** 7467–7473

[16] Philbin T G, Xiong C and Leonhardt U 2010 Casimir stress in an inhomogeneous medium *Ann. Phys.* **325** 579–595

[17] Hough D H and White R A 1980 The Calculation of Hamaker Constants from Lifshitz Theory with Applications to Wetting Phenomena *Adv. Colloid Interface Sci.* **14** 3–14

[18] Dowling J P 1989 The Mathematics of the Casimir Effect *Math. Mag.* **62** 324–331

[19] Genet C, Lambrecht A and Reynaud S 2000 Temperature dependence of the Casimir effect between metallic mirrors *Phys. Rev. A* **62** 012110 (*Preprint* `arXiv:quant-ph/0002061`)

[20] Born M and Wolf E 1980 *Principles of Optics Electromagnetic Theory of Propagation,Interference and Diffraction of Light* 6th ed (Pergamon Press)

[21] Dzyaloshinskii I E, Lifshitz E M and Pitaevskii L P 1961 The general theory of van der Waals forces *Adv. Phys.* **10** 165–209

[22] Zhou F and Spruch L 1995 van der Waals and retardation (Casimir) interactions of an electron or an atom with multilayered walls *Phys. Rev. A* **52** 297–310

[23] Tomaš M S 2002 Casimir force in absorbing multilayers *Phys. Rev. A* **66** 052103 (*Preprint* `arXiv:quant-ph/0207106`)

[24] Raabe C, Knöll L and Welsch D 2003 Three-dimensional Casimir force between absorbing multilayer dielectrics *Phys. Rev. A* **68** 033810 (*Preprint* `arXiv:quant-ph/0212154`)

[25] Ellingsen S A 2007 Casimir attraction in multilayered plane parallel magnetodielectric systems *J. Phys. A: Math. Gen.* **40** 1951–1961 (*Preprint* `arXiv:quant-ph/0607157`)

[26] Inui N 2008 Casimir Energy of the Evanescent Field between Inhomogeneous Dielectric Slabs *J. Phys. Soc. Jpn.* **77** 084001
[27] Feynman R P and Hibbs A R 1965 *Quantum Mechanics and Path Integrals* (New York: McGraw Hill Book Company)
[28] Mandl F and Shaw G 1984 *Quantum Field Theory* (New York: John Wiley & Sons) ISBN 0471-10509-0
[29] Peskin M E and Schroeder D V 2000 *An Introduction to Quantum Field Theory* (New York: Perseus Books)
[30] Bethe H A 1947 The Electromagnetic Shift of Energy Levels *Phys. Rev.* **72** 339–341
[31] Adachi S 1992 *Physical Properties of III-V Semiconductor Compounds* (New York: John Wiley & Sons)
[32] Mason W 1966 *Crystal Physics of Interaction Processes* (New York, London: Academic Press)
[33] Ikeda T 1990 *Fundamentals of Piezoelectricity* (Oxford, New York, Tokyo: Oxford Univ. Press)
[34] Auld B 1973 *Acoustic Fields and Waves in Solids* (New York: John Wiley & Sons)
[35] Wang X, Song J, Liu J and Wang Z L 2007 Direct-Current Nanogenerator Driven by Ultrasonic Waves *Science* **316** 102–105
[36] Bloembergen N 1982 Nonlinear optics and spectroscopy *Rev. Mod. Phys.* **54** 685–695
[37] Zhu T C, Maris H J and Tauc J 1991 Attenuation of longitudinal-acoustic phonons in amorphous SiO_2 at frequencies up to 440 GHz *Phys. Rev. B* **44** 4281–4289
[38] Spencer E G, Lenzo P V and Nassau K 1965 Elastic Wave Propagation in Lithium Niobate *Appl. Phys. Lett.* **7** 67–69
[39] Laermans C 1979 Saturation of the 9.4-GHz Hypersonic Attenuation in Fast-Neutron-Irradiated Crystalline Quartz *Phys. Rev. Lett.* **42** 250–254
[40] Morath C J and Maris H J 1996 Phonon attenuation in amorphous solids studied by picosecond ultrasonics *Phys. Rev. B* **54** 203–213
[41] Weis O 1975 Surface excitation of hypersound in piezoelectric crystals by plane electromagnetic waves *Z. Phys. B: Condens. Matter* **21** 1–10